Computers, Materials & Continua

Tech Science Press

Doi:10.32604/cmc.2025.061071

REVIEW

A Review of the Numerical Methods for Diblock Copolymer Melts

Youngjin Hwang, Seungyoon Kang and Junseok Kim*

Department of Mathematics, Korea University, Seoul, 02841, Republic of Korea

*Corresponding Author: Junseok Kim. Email: cfdkim@korea.ac.kr

Received: 16 November 2024; Accepted: 20 January 2025; Published: 17 February 2025

ABSTRACT: This review paper provides a comprehensive introduction to various numerical methods for the phase-field model used to simulate the phase separation dynamics of diblock copolymer melts. Diblock copolymer systems form complex structures at the nanometer scale and play a significant role in various applications. The phase-field model, in particular, is essential for describing the formation and evolution of these structures and is widely used as a tool to effectively predict the movement of phase boundaries and the distribution of phases over time. In this paper, we discuss the principles and implementations of various numerical methodologies for this model and analyze the strengths, limitations, stability, accuracy, and computational efficiency of each method. Traditional approaches such as Fourier spectral methods, finite difference methods and alternating direction explicit methods are reviewed, as well as recent advancements such as the invariant energy quadratization method and the scalar auxiliary variable scheme are also presented. In addition, we introduce examples of the phase-field model, which are fingerprint image restoration and 3D printing. These examples demonstrate the extensive applicability of the reviewed methods and models.

KEYWORDS: Nonlocal cahn–hilliard; phase-field; diblock copolymer melts; Ohta–Kawasaki model; numerical methods; pattern formation

1 Introduction

In this review, we present an overview of the numerical methodologies for diblock copolymer melts. The Ohta–Kawasaki equation, introduced by Ohta et al. [1], was originally developed to explain the microphase separation patterns in diblock copolymer melts. A diblock copolymer is defined as a polymer composed of two distinct subchains linked by a covalent bond, with each subchain composed of monomers that repel each other. When a large number of such molecules aggregate, they form a structure known as a melt. These diblock copolymer melts are of great interest in both scientific and engineering fields due to their unique phase separation behavior. Their distinct constituent monomers separate to form nanoscale structures with desirable properties [2]. This phase separation is a process known as spinodal decomposition, which enables the formation of various microstructures such as lamellar, cubic, hexagonal, and gyroid configurations depending on the synthetic conditions used [3]. These diverse structures can significantly influence the mechanical properties of the material [4], and it is therefore essential to anticipate the structure that will be formed experimentally.

Due to these unique characteristics, diblock copolymer melts have found applications across multiple fields, such as materials science [5,6], nanotechnology [7–9], and biomedical engineering [10]. Controlled pattern formation at the nanoscale can improve the mechanical, optical, and electrical properties of materials, and enable the creation of advanced materials tailored for specific functions [11]. Several computational

algorithms have been proposed to analyze the equilibrium state of diblock copolymers. Techniques such as Monte Carlo methods [12–14], molecular dynamics [15], self-consistent field theory [16,17], cell dynamics simulations [18], dissipative particle dynamics simulations [19–21] and the phase-field model [22–24] are widely used for this purpose. The phase-field model, in particular, is a continuum model that describes the interface using the order parameter. This model is advantageous because it bypasses the need to solve complex boundary value problems, as it formulates the governing equations through the variation of an energy functional. Consequently, the phase-field model has become a widely adopted approach for reproducing various material structures, and it enables researchers to derive the governing equations in a relatively straightforward manner [25–27]. Researchers also constructed new or modified phase field equations for the diblock copolymer solutions for specific conditions and cases. Shen et al. [28] proposed a thermodynamically consistent phase field equation for the simulation of diblock copolymers. The electric and magnetic field is coupled in the proposed model. The authors constructed the phase field model based on the Onsager principle. In order to solve the proposed model, the energy quadratization technique is applied, while the thermodynamical consistency is preserved. Numerical simulations showed convergence rate of the proposed algorithm and the effects of electric fields and magnetic field on the diblock copolymer system.

The Cahn–Hilliard (CH) equation is a fundamental governing equation in phase-field models and is widely used to describe phase separation phenomena in binary systems. It effectively models the evolution of the compositional concentration field and reveals the role of interface thickness in structure dynamics. The Navier–Stokes equations can model the flow of phases, and various numerical methods have been developed for their solutions [29]. When coupled with the CH equation, the Navier–Stokes equations can be used to model the flow of polymer melts. Song et al. [30] introduced an innovative, unconditionally energy-stable data assimilation algorithm for solving the Navier–Stokes–Cahn–Hilliard equations. Their approach demonstrated robust performance in handling locally discrete observational data. Song et al. [31] proposed an unconditionally energy-stable numerical method for the CH equation and validated its efficiency and stability through numerical experiments involving complex initial conditions. The CH equation is frequently coupled with other equations to capture additional characteristics. Martínez–Agustín et al. [32] proposed coupling the CH equation with the Swift–Hohenberg equation in 3D to model phase transitions in diblock copolymers. The proposed method is solved using the fast Fourier transform and a pseudo-spectral implicit method. Since the model dynamics can produce various morphologies, the porous polymeric materials obtained from numerical simulations have potential applications in 3D printing. As the Ohta–Kawasaki model explains the microphase separation patterns in diblock copolymer melts, Barua et al. [33] rescaled the Ohta–Kawasaki model, free energy, and boundary conditions for more efficient calculations of sharp-interfacial symmetric diblock copolymer problem. They applied boundary integral formulation and small-scale decomposition to solve the governing equations numerically. Their simulations illustrate the evolution of the system from the initial to intermediate states and eventually to the steady. Meng et al. [34] proposed a solution for the nonlocal CH equation with a nonlocal diffusion operator by using a scalar auxiliary variable method. Their proposed methods are unconditionally stable and showed high-order accuracy. Numerical solutions were efficiently obtained using the fast Fourier transform and gradient approach to achieve low storage cost and calculation time. The nonlocal CH equation with degenerate mobility was studied by Elbar et al. [35], where the additional nonlocal term accounts for the surface tension to model long-range interactions.

The Ohta–Kawasaki model, defined on the domain $\Omega \in \mathbb{R}^d$ for $d = 1, 2, 3$, is given by

$$\frac{\partial \phi(\mathbf{x}, t)}{\partial t} = \Delta \mu(\mathbf{x}, t) - \alpha(\phi(\mathbf{x}, t) - \bar{\phi}), \tag{1}$$

$$\mu(\mathbf{x}, t) = F'(\phi(\mathbf{x}, t)) - \varepsilon^2 \Delta \phi(\mathbf{x}, t), \tag{2}$$

where $\phi = \rho_A - \rho_B$ is a phase-field variable representing the local volume fraction of two monomers and $\bar{\phi} = \int_\Omega \phi(\mathbf{x}, 0)/\int_\Omega d\mathbf{x}$. The parameter α is the molecular chain length and ε is the suitably rescaled interfacial thickness at the different two monomer intersections. The term $F(\phi) = 0.25(\phi^2 - 1)^2$ denotes the Helmholtz free energy functional. If $\alpha > 0$, the nonlocal Cahn–Hilliard (NCH) equation becomes the Ohta–Kawasaki model. The total free energy $\mathscr{E}(\phi)$ of the Ohta–Kawasaki model can divided into the short-range energy $\mathscr{E}_s(\phi)$ and long-range energy $\mathscr{E}_l(\phi)$, defined as follows:

$$\mathscr{E}_s(\phi) = \int_\Omega \left(F(\phi) + \frac{\varepsilon^2}{2}|\nabla\phi|^2 \right) d\mathbf{x}, \tag{3}$$

$$\mathscr{E}_l(\phi) = \frac{\alpha}{2}\int_\Omega \int_\Omega G(\mathbf{x}-\mathbf{y})(\phi(\mathbf{x}) - \bar{\phi})(\phi(\mathbf{y}) - \bar{\phi}) d\mathbf{y} d\mathbf{x}, \tag{4}$$

where G is a Green's function [36]. We can rewrite the long-range energy by considering the periodic or zero Neumann boundary conditions.

$$\mathscr{E}_l(\phi) = \frac{\alpha}{2}\int_\Omega \Delta_{\mathbf{x}}\omega(\mathbf{x}) \left[\int_\Omega \Delta_{\mathbf{y}} G(\mathbf{x}-\mathbf{y})\omega(\mathbf{y}) \right] d\mathbf{x} = \frac{\alpha}{2}\int_\Omega |\nabla\omega(\mathbf{x})|^2 d\mathbf{x}, \tag{5}$$

where $\Delta\omega = -(\phi - \bar{\phi})$ and ω is derived from $\Delta\omega$. The total free energy is obtained by summing the short-range and long-range energies.

$$\mathscr{E}(\phi) = \int_\Omega \left(F(\phi) + \frac{\varepsilon^2}{2}|\nabla\phi|^2 + \frac{\alpha}{2}|\nabla\omega|^2 \right) d\mathbf{x}. \tag{6}$$

We also obtain the following energy dissipation law and mass conservation property [37].

$$\begin{aligned} \frac{d}{dt}\mathscr{E}(\phi) &= \int_\Omega \left[\left(F'(\phi) - \varepsilon^2\Delta\phi \right)\phi_t - \alpha\omega\Delta\omega_t \right) d\mathbf{x} \\ &= \int_\Omega (\mu + \alpha\omega)\phi_t d\mathbf{x} = -\int_\Omega |\nabla(\mu + \alpha\omega)|^2 d\mathbf{x} \le 0, \end{aligned} \tag{7}$$

and

$$\begin{aligned} \frac{d}{dt}\int_\Omega \phi d\mathbf{x} &= \int_\Omega \left[\Delta\mu - \alpha(\phi - \bar{\phi}) \right] d\mathbf{x} \\ &= \int_{\partial\Omega} \frac{\partial\mu}{\partial\mathbf{n}} d\mathbf{s} - \alpha\int_\Omega (\phi - \bar{\phi}) d\mathbf{x} = 0, \end{aligned} \tag{8}$$

where the integral by parts and periodic or zero Neumann boundary conditions are applied. Therefore, the Ohta–Kawasaki model satisfies the energy dissipation law and mass conservation by Eqs. (7) and (8), respectively. Because of these two fundamental properties of the Ohta–Kawasaki model, it is natural and important to construct proper numerical schemes that still satisfy these two properties in discrete manners. Singh et al. [9] developed a thermodynamically consistent nonlocal model for phase transformation and heat transfer in block copolymer directed self-assembly using the continuum theory of mixtures. Their model incorporates mass and energy balances, microforce balances, and constitutive relations to couple the phase field and temperature.They developed a finite element solution incorporating stable time-stepping schemes and performed computational tests to validate the equation's effectiveness in simulating the self-assembly behavior of block copolymers. Chen et al. [38] proposed an efficient leapfrog time-marching method for the phase-field diblock copolymer equation, which significantly reduces the computational cost by requiring only the solution of a linear algebra system at each time step, ensures unconditional energy stability for large

time steps, and guarantees the existence and uniqueness of the computational solution at each step, ensuring both reliability and accuracy. This method consists of the leapfrog integration scheme for time discretization and the Fourier spectral method for spatial discretization. The authors analyze the energy dissipation and mass conservation of the proposed numerical method for the Ohta–Kawasaki model and prove that the numerical scheme satisfies both properties. Li et al. [39] developed a highly efficient computational method for a flow-coupled phase-field equation for diblock copolymer melts. This model represents a complex nonlinear system consisting of the Navier–Stokes equations coupled with the CH type equation with an Ohta–Kawasaki potential. By combining decoupling techniques with the projection method, the authors developed a fully decoupled, energy-stable, second-order time-accurate computational method for the model. The decoupling technique is based on designing an auxiliary ordinary differential equation (ODE) that plays a critical role in achieving a fully decoupled structure while maintaining energy stability. The authors rigorously proved that the method satisfies unconditional energy stability. Diblock copolymers under various conditions are studied by Wang et al. [40], authors simulated a hydrodynamically coupled diblock copolymer in complex domains using a diffusion domain method which efficiently overcomes the problems derived from complex boundaries. Therefore, the computational efficiency is highly increased. In addition, 2D and 3D models are also considered using the second-order dimension splitting technique, which allows multi dimension problems to be decomposed into a 1D problem. Various numerical simulation tests in 1D, 2D and 3D verified the stability, accuracy and efficiency of the proposed method. The Hele–Shaw cell simulates a flow in a narrow gap between two flat parallel plates, which can model interfacial pattern formation in nonequilibrium systems [41]. Modeling a diblock copolymer melt in the Hele-Shaw cell is a complicated nonlinear system. Cao et al. [42] studied this system using a combination of explicit-invariant energy quadratization and projection methods. The proposed method is second order accurate in time and energy stable. Due to the introduction of two auxiliary variables, high efficiency is also achieved. Numerical simulations with random initial conditions confirmed various characteristics of the proposed method such as accuracy, stability. The spinodal decomposition in the rotating Hele–Shaw cell is also simulated using the proposed scheme. Xu et al. [43] studied the evolution of diblock copolymer in 2D domain where the governing equation is the extended Ohta–Kawasaki model. The projection operator is introduced to achieve mass conservation property of the proposed method. The projection method is constructed with a small computational cost, therefore simplifying the numerical algorithm. Zhang et al. [44] studied the microphase separation of diblock copolymers in three-dimensional space using a modified NCH equation, which is a variant of the CH equation with a viscous term. The viscous term introduces viscous effects to the governing equation. The integrating factor Runge–Kutta technique is adopted for large tie-stepping. Numerical simulation of diblock copolymers in 3D shows that the proposed scheme is capable of distinguishing different phase geometries. The maximum principle, mass conservation and energy stability is also satisfied in this numerical test. Luo et al. [45] studied the 2D and 3D nonlocal Ohta–Kawasaki model using the Fourier spectral method, where the nonlocal Ohta–Kawasaki model studies the pattern formation for the diblock copolymer system. The second-order backward finite difference method (FDM) is applied for Fourier collocation discretization. The asymptotic compatibility of the method is mainly discussed in this paper, proving in both analytic and numerical approaches. Numerical simulations also confirmed characteristics of the proposed method such as upper boundedness, effect of parameters, convergence rate and energy stability. Iqbal et al. [46] introduced a cell dynamic simulation model that predicts simulation outcomes through an examination of flow, deformation, and phase transitions in diblock copolymer systems under curvilinear coordinate systems.

In this review, we focus on various numerical methods and applications for solving the NCH equation for microphase separation patterns in diblock copolymer melts. The overall structure of the paper is as

follows. Section 2 presents detailed explanations of the various numerical schemes for solving the NCH equation. Section 3 introduces the applications of the phase-field model for diblock copolymer melts. Section 4 presents the conclusion.

2 Numerical Methods

We describe the various numerical methods used to solve the NCH equation. We consider the computational domain $\Omega = (L_x, R_x) \times (L_y, R_y)$ in 2D space. Let Δt be time step. We define $h = (R_x - L_x)/N_x = (R_y - L_y)/N_y$. The discrete domain is defined as $\Omega^d = \{(x_i = L_x + ih, y_j = L_y + jh) \mid i = 0, 1, \ldots, N_x, \quad j = 0, 1, \ldots, N_y\}$ or $\Omega^d = \{(x_i = L_x + (i - 0.5)h, y_j = L_y + (j - 0.5)h) \mid i = 1, 2, \ldots, N_x, j = 1, 2, \ldots, N_y\}$ depending on whether we use cell corner points or cell center points. Fig. 1 shows the schematic illustrations of the cell corner points and cell center points on the computational domain. In this review paper, when boundary conditions are not explicitly specified, a periodic boundary condition is applied for a discrete domain with cell corner points, as shown in Fig. 1a, while a Neumann boundary condition is applied for a discrete domain with cell center points, as shown in Fig. 1b. Let ϕ_{ij}^n be the approximation of the $\phi(x_i, y_j, n\Delta t)$. The discrete l_2-norm in is defined by

$$\|\phi\|_2 = \sqrt{\frac{1}{N_x N_y} \sum_{i=1}^{N_x} \sum_{j=1}^{N_y} (\phi_{ij})^2}.$$

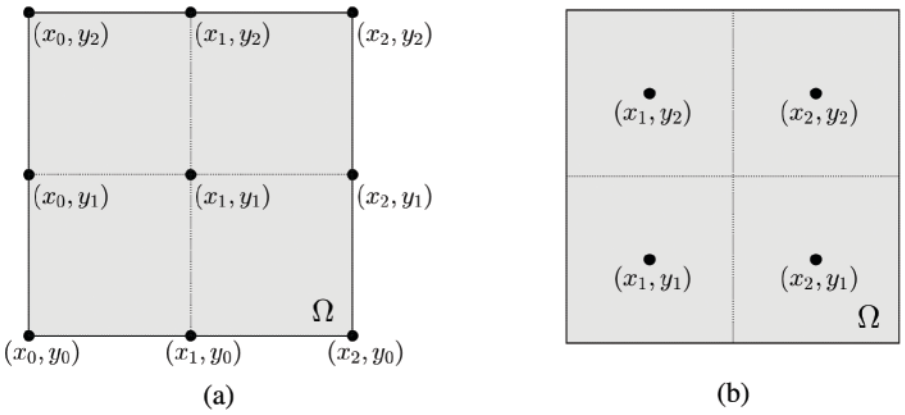

Figure 1: Schematic illustrations of (a) cell corner points and (b) cell center points on the computational domain

We can easily reduce or extend to one-dimensional and three-dimensional spaces.

When reviewing the numerical methods, we mainly focus on the accuracy and stability of the reviewed methods. High accuracy allows the user to predict phase separation dynamics in diblock copolymer systems with relatively low computational cost, such as coarse spatial grid or large time step. Therefore, high accuracy can lead to an effective numerical method. Stability is also concerned with time step and accuracy of the numerical method. High stability, and sometimes unconditional stability allows a larger time step to be used for the numerical simulation without the risk of blowing up. Therefore, we can obtain more freedom when modifying the time step size for a desired accuracy.

2.1 Finite Difference Method

The FDM is a widely employed numerical technique for solving partial differential equations, known for its simplicity and broad applicability. A key advantage of this method is its ease of implementation for a range of problems with regular grid structures, making it particularly effective for time-dependent simulations. Although the accuracy of the method is influenced by grid resolution and step size, it can be refined to achieve higher precision. Despite some limitations in handling complex boundaries or irregular domains, the FDM remains a valuable tool due to its computational efficiency and straightforward implementation. Xiao et al. [47] developed a space-time fourth-order method for two- and three-dimensional CH type equations. The authors used the operator splitting method with auxiliary variables for spatial differentiation terms to enable multi-thread computation. In addition, we extended the numerical scheme for the phase-field diblock copolymer model. Numerical methods for solving systems of equations with nonlinear terms, such as the NCH equation, are primal and difficult problems [48]. Jeong et al. [22] conduct a numerical investigation on controlling local defectivity in self-assembled diblock copolymer patterns by designing suitable substrates. The numerical solution algorithm is described as follows. Considering trench domain Ω with boundaries $\partial\Omega_1$ and $\partial\Omega_2$ shown in Fig. 2. For ϕ, we use the Dirichlet and periodic boundary conditions in $\partial\Omega_1$ and $\partial\Omega_2$, respectively. For μ, we apply the Neumann and periodic boundary conditions in $\partial\Omega_1$ and $\partial\Omega_2$, respectively.

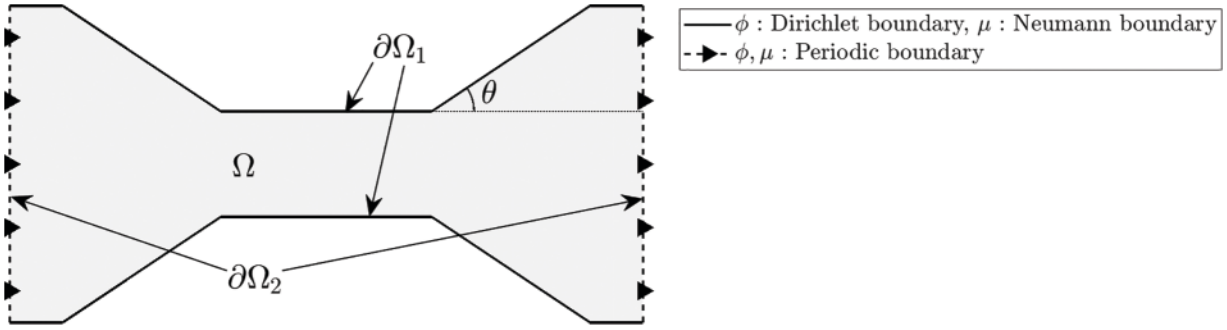

Figure 2: Schematic diagram of the computational domain Ω with boundaries $\partial\Omega_1$ and $\partial\Omega_2$

We discretize Ω using cell corner points. The NCH Eqs. (1) and (2) with non-linearly stabilized splitting scheme [49] is rewritten as

$$\frac{\phi_{ij}^{n+1}-\phi_{ij}^{n}}{\Delta t}=\Delta\mu_{ij}^{n+1}-\alpha\left(\phi_{ij}^{n+1}-\bar{\phi}\right), \tag{9}$$

$$\mu_{ij}^{n+1}=(\phi_{ij}^{n+1})^3-\phi_{ij}^{n}-\varepsilon^2\Delta\phi_{ij}^{n+1}, \tag{10}$$

where $\bar{\phi}=\sum_{\mathbf{x}_{ij}\in\Omega}\phi_{ij}^{0}/\sum_{\mathbf{x}_{ij}\in\Omega}1$. To solve the NCH Eqs. (9) and (10), we apply the Gauss–Seidel iterative scheme. Given ϕ_{ij}^{n}, let $\phi_{ij}^{n+1,0}=\phi_{ij}^{n}$ be an initial guess. We calculate $\phi_{ij}^{n+1,m+1}$ and $\mu_{ij}^{n+1,m+1}$ from $\phi_{ij}^{n+1,m}$ and $\mu_{ij}^{n+1,m}$ for $m=0,1,\ldots$ by

$$\left(\frac{1}{\Delta t}+\alpha\right)\phi_{ij}^{n+1,m+1}+\frac{4}{h^2}\mu_{ij}^{n+1,m+1} \tag{11}$$
$$=\frac{\phi_{ij}^{n}}{\Delta t}+\alpha\bar{\phi}+\frac{\mu_{i-1,j}^{n+1,m+1}+\mu_{i+1,j}^{n+1,m}+\mu_{i,j-1}^{n+1,m+1}+\mu_{i,j+1}^{n+1,m}}{h^2},$$

$$\left(-\frac{4\varepsilon^2}{h^2} - 3(\phi_{ij}^{n+1,m})^2\right)\phi_{ij}^{n+1,m+1} + \mu_{ij}^{n+1,m+1} \tag{12}$$
$$= -\phi_{ij}^{n} - 2(\phi_{ij}^{n+1,m})^3 - \varepsilon^2 \frac{\phi_{i-1,j}^{n+1,m+1} + \phi_{i+1,j}^{n+1,m} + \phi_{i,j-1}^{n+1,m+1} + \phi_{i,j+1}^{n+1,m}}{h^2}.$$

We need to apply certain special formulas considering the boundary conditions. To facilitate understanding, we consider one example illustrated in Fig. 3. For the points ϕ_{ij} near the boundary within the domain Ω, the values of ϕ_a and ϕ_b at $\partial\Omega_1$, as shown in Fig. 3a, are determined by the Dirichlet boundary condition and correspond to the maximum values of the numerical equilibrium solution, $\|\phi^{eq}\|_\infty$. Moreover, as shown in Fig. 3b, the values of μ_a and μ_b at $\partial\Omega_1$ are determined by the Neumann boundary condition and correspond to μ_p and μ_q, respectively, which are obtained by the linear interpolation of neighboring points. Thus, $\mu_a = \mu_q$ and $\mu_b = \mu_p$. Here, μ_a and μ_p have the same values and are located at distinct positions. Similarly, μ_b and μ_q also share identical values and are situated at separate locations. Other points near the boundary are similar. We can obtain the values of ϕ_a and ϕ_b at the boundary $\partial\Omega_1$ using the Dirichlet boundary condition. We define the numerical equilibrium solution as ϕ^k if $\|\phi^k - \phi^{k-1}\|_2 \le 10^{-6}$ for $k \ge 1$. The discrete second derivatives near boundary for the Dirichlet boundary condition are defined by

$$\Delta_{xx}^D \phi_{ij} = \left(\frac{\phi_a - \phi_{ij}}{\alpha h} - \frac{\phi_{ij} - \phi_{i-1,j}}{h}\right) \Bigg/ \left(\frac{\alpha h + h}{2}\right),$$
$$\Delta_{yy}^D \phi_{ij} = \left(\frac{\phi_b - \phi_{ij}}{\beta h} - \frac{\phi_{ij} - \phi_{i,j-1}}{h}\right) \Bigg/ \left(\frac{\beta h + h}{2}\right),$$

where ϕ_a and ϕ_b are the maximum values of the numerical equilibrium solution and $0 < \alpha, \beta < 1$. Then, for the Dirichlet boundary condition, we define the discrete Laplace operator as $\Delta^D \phi_{ij}^{n+1} = \Delta_{xx}^D \phi_{ij}^{n+1} + \Delta_{yy}^D \phi_{ij}^{n+1}$. Next, we define the discrete second derivatives near boundary for the Neumann boundary condition as

$$\Delta_{xx}^N \mu_{ij} = \left(\frac{\mu_a - \mu_{ij}}{\alpha h} - \frac{\mu_{ij} - \mu_{i-1,j}}{h}\right) \Bigg/ \left(\frac{\alpha h + h}{2}\right),$$
$$\Delta_{yy}^N \mu_{ij} = \left(\frac{\mu_b - \mu_{ij}}{\beta h} - \frac{\mu_{ij} - \mu_{i,j-1}}{h}\right) \Bigg/ \left(\frac{\beta h + h}{2}\right),$$

where $\mu_a = \mu_p = p\mu_{ij} + (1-p)\mu_{i,j-1}$ and $\mu_b = \mu_q = (1-q)\mu_{ij} + q\mu_{i-1,j}$ by the linear interpolation. Therefore, for the Neumann boundary condition, the discrete Laplace operator is defined by $\Delta^N \mu_{ij}^{n+1} = \Delta_{xx}^N \mu_{ij}^{n+1} + \Delta_{yy}^N \mu_{ij}^{n+1}$. We repeat the above iterations until the l_2-norm error between numerical solutions at successive time steps is smaller than a given tolerance tol: $\|\phi^{n+1,m+1} - \phi^{n+1,m}\|_2 < tol$. We perform the numerical simulations using the parameters $L^* = 0.375$, $h = L^*/10$, $N_x = 500$, $N_y = 300$, $\Delta t = 0.1h$, $\varepsilon = 1/(25\sqrt{2})$, $\alpha = 100$, the maximum values of the numerical equilibrium solution $\|\phi^{eq}\|_\infty = 0.6134$. The initial condition on the computational domain $\Omega = (-25L^*, 25L^*) \times (-15L^*, 15L^*)$ is defined as $\phi(x, y, 0) = 0.01\text{rand}(x, y)$. Fig. 4 shows the numerical solution solved using the numerical method [22].

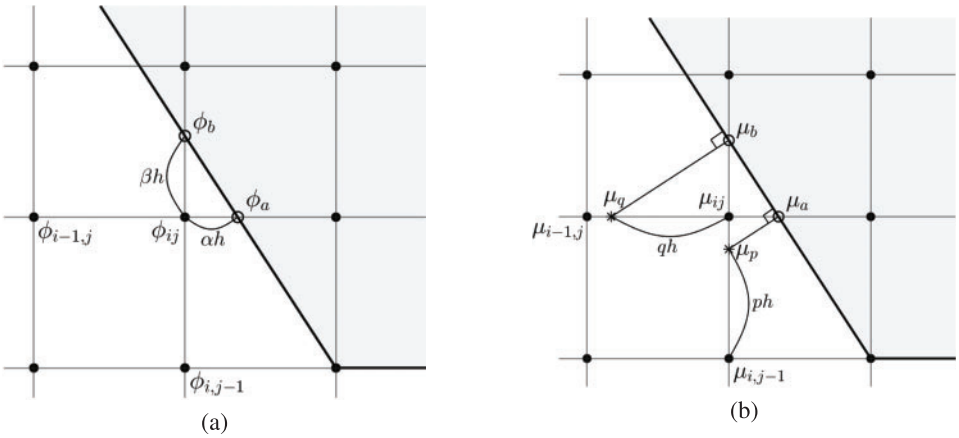

Figure 3: Schematic representation of (a) Dirichlet boundary condition and (b) Neumann boundary condition

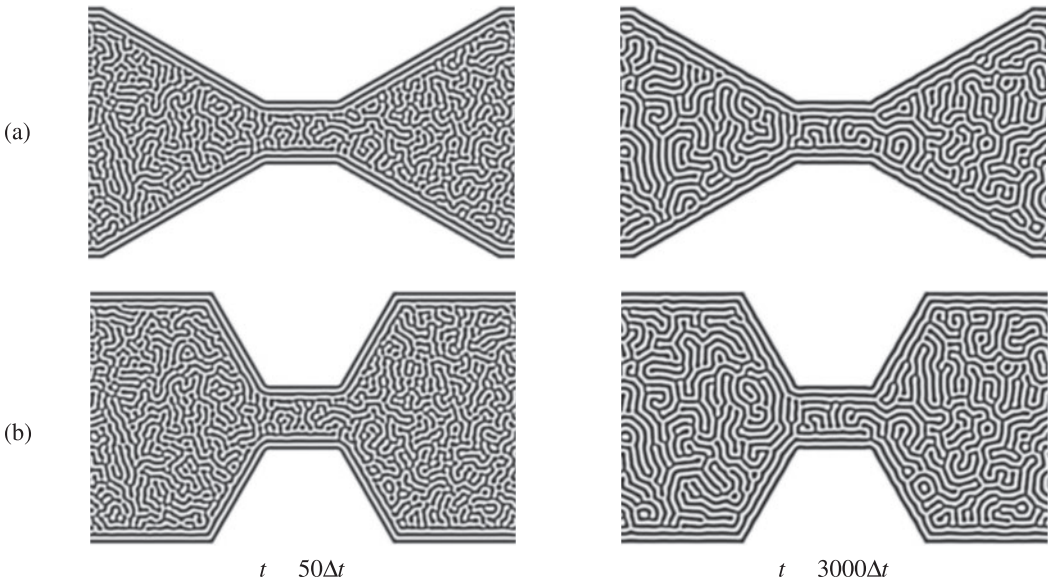

Figure 4: Snapshots of the numerical solutions with (a) $\theta = 30$ and (b) $\theta = 60$

Jeong et al. [24] developed a numerical method to investigate microphase separation patterns in diblock copolymer melts on curved surfaces. This method employs a discrete narrow band grid adjacent to the curved surface and applies a pseudo-Neumann boundary condition for the near boundary using the closest point scheme. Therefore, the Laplace–Beltrami operator can be replaced with the standard Laplace operator. We define the σ-neighborhood band domain as $\Omega_\sigma = \{(x, y, z) \mid (a, b, c) \in S, (x, y, z) = (a, b, c) + \theta \mathbf{n}(a, b, c)$ for $|\theta| < \sigma\}$, which includes the surface S. Here, $\mathbf{n}(a, b, c)$ is the unit normal vector at (a, b, c) on the surface S. The global domain that includes the Ω_σ is defined by $\Omega = (L_x, R_x) \times (L_y, R_y) \times (L_z, R_z)$. Let N_x, N_y, and N_z be positive integers and let $h = (R_z - L_z)/N_z = (R_y - L_y)/N_y = (R_x - L_x)/N_x$ be a size of spatial step. The discrete global domain is defined as $\Omega^d = \{(x_i = L_x + ih, y_j = L_y + jh, z_k = L_z + kh) \mid i = 0, 1, \ldots, N_x,\ j = 0, 1, \ldots, N_y, k = 0, 1, \ldots, N_z\}$. Let ϕ^n_{ijk} and μ^n_{ijk} be approximations of $\phi(x_i, y_j, z_k, n\Delta t)$ and $\mu(x_i, y_j, z_k, n\Delta t)$, respectively. The discrete narrow band domain is defined by $\Omega^d_\sigma = \{(x_i, y_j, z_k) : |\psi_{ijk}| < \sigma\}$. To find the boundary points of discrete narrow band domain Ω^d_σ, define $P_{ijk} = 0$ if $(x_i, y_j, z_k) \in \Omega^d_\sigma$ and

$P_{ijk} = 1$ otherwise. Let $\partial\Omega_\sigma^d = \{(x_i, y_j, z_k) : P_{ijk}|\nabla P_{ijk}| \neq 0\}$ be the boundary points of discrete narrow band domain. Here, the gradient of P is defined by

$$\nabla P_{ijk} = \frac{(P_{i+1,jk} - P_{i-1,jk}, P_{i,j+1,k} - P_{i,j-1,k}, P_{ij,k+1} - P_{ij,k-1})}{2h}.$$

We define the discrete Laplace operator as

$$\Delta\phi_{ijk}^n = \frac{\phi_{ij,k+1}^n + \phi_{ij,k-1}^n + \phi_{i,j+1,k}^n + \phi_{i,j-1,k}^n + \phi_{i+1,jk}^n + \phi_{i-1,jk}^n - 6\phi_{ijk}^n}{h^2}.$$

Then, we discretization the NCH Eqs. (1) and (2) by applying the unconditionally stable scheme.

$$\frac{\phi_{ijk}^{n+1} - \phi_{ijk}^n}{\Delta t} = \Delta\mu_{ijk}^{n+1} - \alpha(\phi_{ijk}^{n+1} - \bar{\phi}), \tag{13}$$

$$\mu_{ijk}^{n+1} = (\phi_{ijk}^{n+1})^3 - \phi_{ijk}^n - \varepsilon^2\Delta\phi_{ijk}^{n+1}. \tag{14}$$

The numerical closest point of $\mathbf{x}_{ijk} = (x_i, y_j, z_k)$ on S is defined by

$$cp(\mathbf{x}_{ijk}) = \mathbf{x}_{ijk} - \frac{\nabla|\psi_{ijk}|}{|\nabla|\psi_{ijk}||}|\psi_{ijk}|.$$

We use pseudo-Neumann boundary condition on $\partial\Omega_\sigma^d$ as

$$\phi_{ijk}^{n+1} = \phi^{n+1}\left(cp(\mathbf{x}_{ijk})\right) \text{ and } \mu_{ijk}^{n+1} = \mu^{n+1}\left(cp(\mathbf{x}_{ijk})\right).$$

Fig. 5a,b shows schematic illustrations of the narrow band domain for the cross section of the sphere in three- and two-dimensions, respectively. Since $cp(\mathbf{x}_{ijk})$ is not included in the grid points above the discrete narrow band domain, we compute $\phi^n(cp(\mathbf{x}_{ijk}))$ using the trilinear interpolation. Then, we solve the discrete NCH equation using the Jacobi iterative method [50], which iteratively updates the solution until convergence. Given ϕ_{ijk}^n and μ_{ijk}^n on Ω_σ^d, the initial guesses $\phi_{ijk}^{n+1,0}$ and $\mu_{ijk}^{n+1,0}$ are used as starting points for the iterative process and are set to ϕ_{ijk}^n and μ_{ijk}^n, respectively. Specifically, $\phi_{ijk}^{n+1,0} = \phi_{ijk}^n$ and $\mu_{ijk}^{n+1,0} = \mu_{ijk}^n$. Then, we calculate the Eqs. (13) and (14) by the following Jacobi iteration for $m \geq 0$.

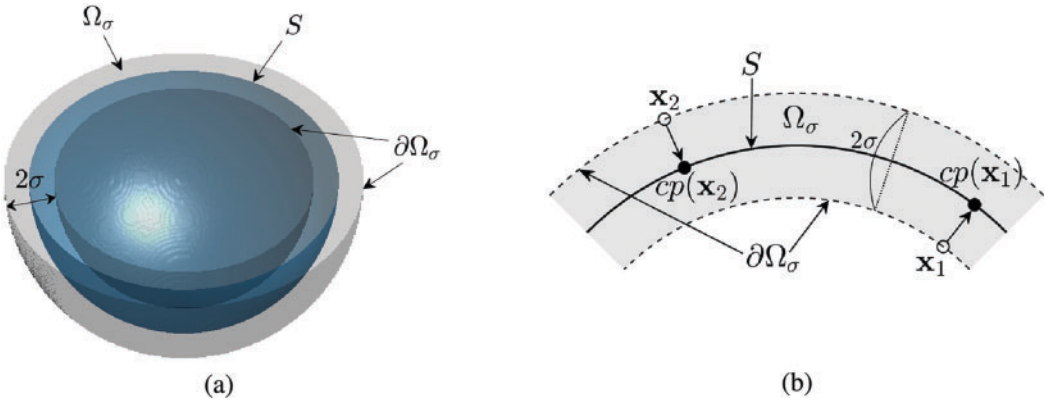

Figure 5: Schematic illustrations of (a) the narrow band domain for surface S and (b) the closest points for the boundary $\partial\Omega_\sigma$ of narrow band domain

$$\left(\frac{1}{\Delta t}+\alpha\right)\phi_{ijk}^{n+1,m+1}+\frac{6}{h^2}\mu_{ijk}^{n+1,m+1}=\frac{\phi_{ijk}^{n}}{\Delta t}+\alpha\bar{\phi}+\frac{1}{h^2}(\mu_{i+1,jk}^{n+1,m}+\mu_{i-1,jk}^{n+1,m}+\mu_{i,j+1,k}^{n+1,m})$$
$$+\frac{1}{h^2}(\mu_{i,j-1,k}^{n+1,m}+\mu_{ij,k+1}^{n+1,m}+\mu_{ij,k-1}^{n+1,m}), \tag{15}$$

$$-\left(3(\phi_{ijk}^{n+1,m})^2+\frac{6\varepsilon^2}{h^2}\right)\phi_{ijk}^{n+1,m+1}+\mu_{ijk}^{n+1,m+1}=-\phi_{ijk}^{n}+2(\phi_{ijk}^{n+1,m})^3+\frac{\varepsilon^2}{h^2}(\phi_{i+1,jk}^{n+1,m}+\phi_{i-1,jk}^{n+1,m})$$
$$+\frac{\varepsilon^2}{h^2}(\phi_{i,j+1,k}^{n+1,m}+\phi_{i,j-1,k}^{n+1,m}+\phi_{ij,k+1}^{n+1,m}+\phi_{ij,k-1}^{n+1,m}), \tag{16}$$

Here, we iteratively compute Eqs. (15) and (16) until $\|\phi^{n+1,m+1}-\phi^{n+1,m}\|_2 < tol$ on Ω_σ^d is satisfied for given tolerance tol. Therefore, we obtain the ϕ_{ijk}^{n+1} on the narrow band domain Ω_σ^d. For more details of the numerical algorithm, the reader is referred to [24].

Fig. 6 displays the temporal evolution of the computational solution for the bunny surface with initial conditions $\phi(\mathbf{x},0)=-0.3+0.1\text{rand}(\mathbf{x})$, $N_x=N_y=N_z=138$, $h=0.031$, $\Delta t=0.1$, $\varepsilon=1/(30\sqrt{2})$, and $\alpha=150$, where rand $(\mathbf{x})$ is the random value from −1 to 1 at the point $\mathbf{x}$.

Figure 6: Snapshot of the numerical solution using the numerical algorithm from [24] at time $t=20\Delta t$, $25\Delta t$, and $600\Delta t$ on the bunny surface

We observe that numerical simulation results form appropriate patterns in complex bunny surfaces. Yang [23] presented a linear time-marching scheme for the Ohta–Kawasaki model coupled with incompressible fluid flow, describing the phase-field model for diblock copolymers in fluid environments. The numerical algorithm employs the scalar auxiliary variable (SAV) approach, which ensures energy stability, even with large time steps. The 2D and 3D spatial discretizations are conducted using the FDM, providing a practical and efficient framework for computation. Furthermore, the authors analytically demonstrated the existence of unique solutions and proved the method's energy stability.

2.2 Fourier Spectral Method

The Fourier spectral method is a technique for solving partial differential equations, that approximates a solution using a sum of functions from a certain function space. To solve problems with periodic boundary conditions, use Fourier transformation composed of sine and cosine functions, and to solve problems with Neumann boundary conditions, use cosine transformation composed only of cosine functions. We consider only two dimensions, and for one or three dimensions it is easily derived from this. The Fourier

transformation satisfies the periodic boundary condition, thus we define the discrete domain using the cell corner points. The discrete Fourier transform and its inverse transform are defined by

$$\hat{\phi}_{pq}^{n} = \sum_{j=1}^{N_y}\sum_{i=1}^{N_x} \phi_{ij}^{n} e^{-i(x_i\xi_p + y_j\eta_q)}, \tag{17}$$

$$\phi_{ij}^{n} = \frac{1}{N_x N_y} \sum_{q=1-N_y/2}^{N_y/2} \sum_{p=1-N_x/2}^{N_x/2} \hat{\phi}_{pq}^{n} e^{i(x_i\xi_p + y_j\eta_q)}, \tag{18}$$

where $\xi_p = 2\pi p/(R_x - L_x)$ and $\eta_q = 2\pi q/(R_y - L_y)$. Let $\phi(x, y, n\Delta t)$ be sufficiently smooth continuous extension counterpart of ϕ_{ij}^{n}. The partial derivatives in Fourier space for the variables x and y are

$$\frac{\partial \phi(x, y, n\Delta t)}{\partial x} = \frac{1}{N_x N_y} \sum_{q=1-N_y/2}^{N_y/2} \sum_{p=1-N_x/2}^{N_x/2} (i\xi_p)\hat{\phi}(\xi_p, \eta_q, n\Delta t) e^{i(\xi_p x + \eta_q y)}, \tag{19}$$

$$\frac{\partial \phi(x, y, n\Delta t)}{\partial y} = \frac{1}{N_x N_y} \sum_{q=1-N_y/2}^{N_y/2} \sum_{p=1-N_x/2}^{N_x/2} (i\eta_q)\hat{\phi}(\xi_p, \eta_q, n\Delta t) e^{i(\xi_p x + \eta_q y)}. \tag{20}$$

Thus, Laplacian is defined using Eqs. (19) and (20) as

$$\begin{aligned}\Delta\phi(x, y, n\Delta t) &= \frac{\partial^2 \phi(x, y, n\Delta t)}{\partial x^2} + \frac{\partial^2 \phi(x, y, n\Delta t)}{\partial y^2} \\ &= -\frac{1}{N_x N_y} \sum_{q=1}^{N_y}\sum_{p=1}^{N_x} \left(\xi_p^2 + \eta_q^2\right) \hat{\phi}(\xi_p, \eta_q, n\Delta t) e^{i(\xi_p x + \eta_q y)}.\end{aligned}$$

Then, the linearly stabilized splitting method is used to the NCH equation as

$$\frac{\phi_{ij}^{n+1} - \phi_{ij}^{n}}{\Delta t} = \Delta\left(2\phi_{ij}^{n+1} + f_{ij}^{n} - \varepsilon^2(\Delta\phi^{n+1})_{ij}\right)_{ij} - \alpha\left(\phi_{ij}^{n+1} - \bar{\phi}\right), \tag{21}$$

where $f_{ij}^{n} = (\phi_{ij}^{n})^3 - 3\phi_{ij}^{n}$. Thus, we applied the discrete Fourier transformation to Eq. (21).

$$\frac{\hat{\phi}_{pq}^{n+1} - \hat{\phi}_{pq}^{n}}{\Delta t} = -\left(\xi_p^2 + \eta_q^2\right)\left(2\hat{\phi}_{pq}^{n+1} + \varepsilon^2(\xi_p^2 + \eta_q^2)\hat{\phi}_{pq}^{n+1} + \hat{f}_{pq}^{n}\right) - \alpha\left(\hat{\phi}_{pq}^{n+1} - \bar{\phi}\right). \tag{22}$$

Hence, we obtain the numerical solution in the Fourier space from Eq. (22) as

$$\hat{\phi}_{pq}^{n+1} = \frac{\hat{\phi}_{pq}^{n} + \Delta t\left(\alpha\bar{\phi}\hat{\mathbf{1}}_{pq} - (\xi_p^2 + \eta_q^2)\hat{f}_{pq}^{n}\right)}{1 + \Delta t\left(\alpha + 2(\xi_p^2 + \eta_q^2) + \varepsilon^2(\xi_p^2 + \eta_q^2)^2\right)}.$$

Then, we use the inverse discrete Fourier transform to obtain the computational solution ϕ_{ij}^{n} for $i = 1, 2, \ldots, N_x$, $j = 1, 2, \ldots, N_y$.

$$\phi_{ij}^{n+1} = \frac{1}{N_x N_y} \sum_{q=1-N_y/2}^{N_y/2} \sum_{p=1-N_x/2}^{N_x/2} \hat{\phi}_{pq}^{n+1} e^{i(x_i\xi_p + y_j\eta_q)}.$$

The Fourier spectral method based on discrete cosine transformation can be used to solve phase-field models with Neumann boundary conditions [51]. We define the computational discrete domain using the

cell center points to describe the Fourier spectral method with discrete cosine transform. The discrete cosine transform and its inverse transform are defined by

$$\hat{\phi}^n_{pq} = u_p v_q \sum_{j=1}^{N_y}\sum_{i=1}^{N_x} \phi^n_{ij} \cos\left(\xi_p \hat{x}_i\right) \cos\left(\eta_q \hat{y}_j\right)$$

$$\phi^n_{ij} = \sum_{q=1}^{N_y}\sum_{p=1}^{N_x} u_p v_q \hat{\phi}^n_{pq} \cos\left(\xi_p \hat{x}_i\right) \cos\left(\eta_q \hat{y}_j\right),$$

where $\hat{x}_i = x_i - L_x$, $\hat{y}_j = y_j - L_y$, $\xi_p = \pi(p-1)/(R_x - L_x)$, $\eta_q = \pi(q-1)/(R_y - L_y)$, $u_1 = \sqrt{1/N_x}$, $v_1 = \sqrt{1/N_y}$, $u_p = \sqrt{2/N_x}$ for $p = 2, 3, \ldots, N_x$, and $v_q = \sqrt{2/N_y}$ for $q = 2, 3, \ldots, N_y$. Therefore, the partial derivatives in the Fourier space for the variables x and y are defined by

$$\frac{\partial \phi(x, y, n\Delta t)}{\partial x} = -\sum_{q=1}^{N_y}\sum_{p=1}^{N_x} u_p v_q \xi_p \hat{\phi}(\xi_p, \eta_q, n\Delta t) \sin\left(\xi_p \hat{x}\right) \cos\left(\eta_q \hat{y}\right)$$

$$\frac{\partial \phi(x, y, n\Delta t)}{\partial y} = -\sum_{q=1}^{N_y}\sum_{p=1}^{N_x} u_p v_q \eta_q \hat{\phi}(\xi_p, \eta_q, n\Delta t) \cos\left(\xi_p \hat{x}\right) \sin\left(\eta_q \hat{y}\right),$$

where $\hat{x} = (x - L_x)$ and $\hat{y} = (y - L_y)$. We get the Laplacian by using the partial derivatives in Fourier space:

$$\begin{aligned}\Delta\phi(x, y, n\Delta t) &= \frac{\partial^2 \phi(x, y, n\Delta t)}{\partial x^2} + \frac{\partial^2 \phi(x, y, n\Delta t)}{\partial y^2} \\ &= -\sum_{q=1}^{N_y}\sum_{p=1}^{N_x} \left(\xi_p^2 + \eta_q^2\right) u_p v_q \hat{\phi}(\xi_p, \eta_q, n\Delta t) \cos\left(\xi_p \hat{x}\right) \cos\left(\eta_q \hat{y}\right).\end{aligned}$$

Hence, similar to the Fourier spectral method with discrete Fourier transform, we can solve Eq. (21) using discrete cosine transformation. Xia et al. [52] employed a phase-field model within a Lagrange multiplier framework to investigate crystal phase transitions and nucleation processes, demonstrating the effectiveness of the Fourier spectral method in capturing complex phase dynamics. Li et al. [53] used the Fourier spectral method to solve biological transport networks in complex domains, providing insights into the optimization properties and adaptive mechanisms of network structures. Refer to [54] for detailed information. Fig. 7 shows the schematic illustrations of the discrete Fourier transform, the discrete cosine transform, and the discrete sine transform, from top to bottom. The dots on the x-axis represent the points of the discrete domain, while the dashed lines connecting the dots indicate the corresponding values of $\phi(x)$ and the solid line is the sum of the basis functions for each transformation that includes all the discrete points. We can observe that the curves represent the sums of the bases of each discrete transform, satisfying the respective boundary conditions.

Jeong et al. [55] investigated the energy-minimizing wavelength in the equilibrium state of diblock copolymers in the hex-cylinder phase by solving the NCH equation using the Fourier spectral method with the discrete Fourier transform. The boundary condition is a periodic boundary condition with the discrete domain using the cell center point. The authors performed computations in rectangular domains with an aspect ratio of $\sqrt{3}$ until a numerical equilibrium state was reached, and repeated the calculations in progressively larger domains. Fig. 8 displays the schematic diagram of the hexagonal pattern and the domain with aspect ratio $1:\sqrt{3}$ for the one-period hexagonal pattern.

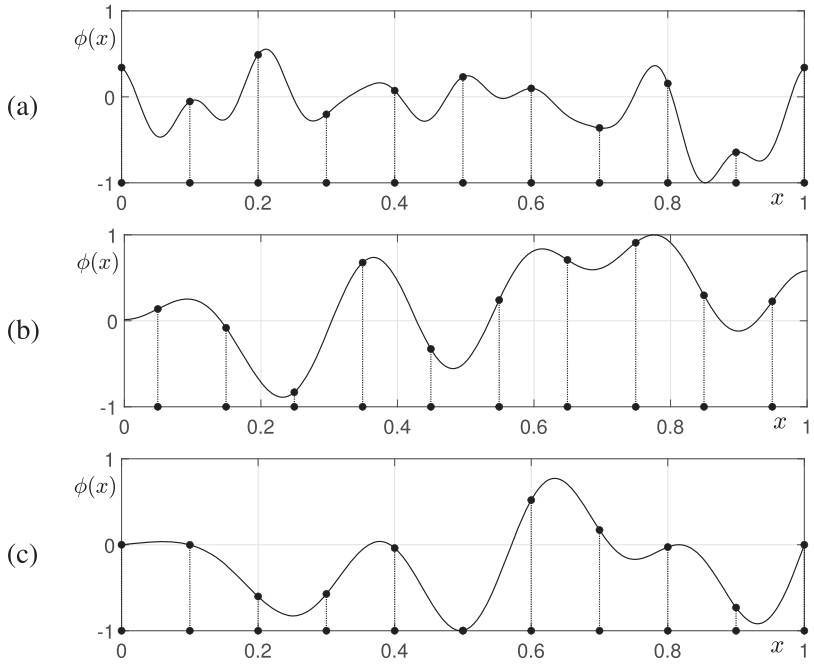

Figure 7: Schematic illustrations of (a) the discrete Fourier, (b) the discrete cosine, and (c) the discrete sine transforms

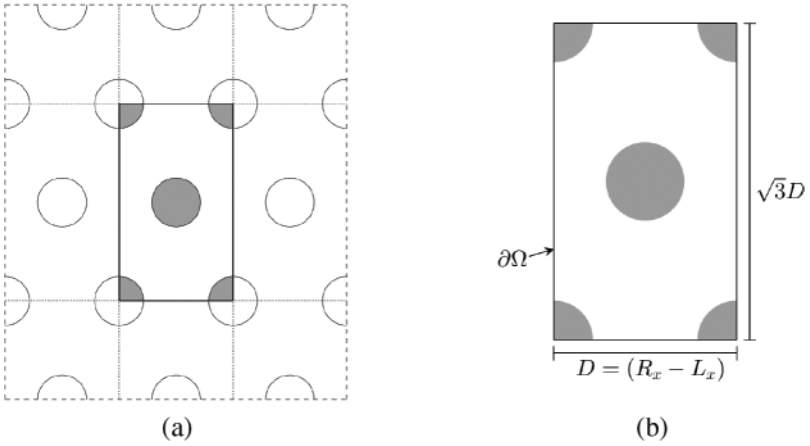

Figure 8: Schematic diagram of (a) the hexagonal pattern and (b) the domain with aspect ratio $1:\sqrt{3}$ for the one-period hexagonal pattern

At time $n\Delta t$, the discrete total energy of the numerical solution for the NCH equation is defined by

$$\mathscr{E}^d(\phi^n) = \sum_{m=1}^{N_x}\sum_{n=1}^{N_y}\left(h^2F(\phi_{ij}^n) + \frac{\varepsilon^2}{2}[(\phi_{i+1,j}^n - \phi_{ij}^n)^2 + (\phi_{i,j+1}^n - \phi_{ij}^n)^2] + \frac{\alpha}{2}\left[(\psi_{i+1,j}^n - \psi_{ij}^n)^2 + (\psi_{i,j+1}^n - \psi_{ij}^n)^2\right]\right).$$

We perform the numerical test for the discrete total energy. For numerical simulation, $\Omega = (0, R_x = h_xN_x) \times (0, R_y = \sqrt{3}R_y)$ is used, where h_x is spatial step size for x-axis. The parameters used $h_x = 0.0015$, $N_x = 512$, $\alpha = 100$, $\Delta t = 0.125$, $\varepsilon = 1/(20\sqrt{2})$. The initial condition is $\phi(x, y, 0) = -0.3 + 0.2\text{rand}(x, y)$ on Ω.

We perform simulations until the computational solution becomes a numerical equilibrium solution. Fig. 9 shows the discrete total energy dissipation and the snapshot of the numerical solutions at the time indicated by the dot.

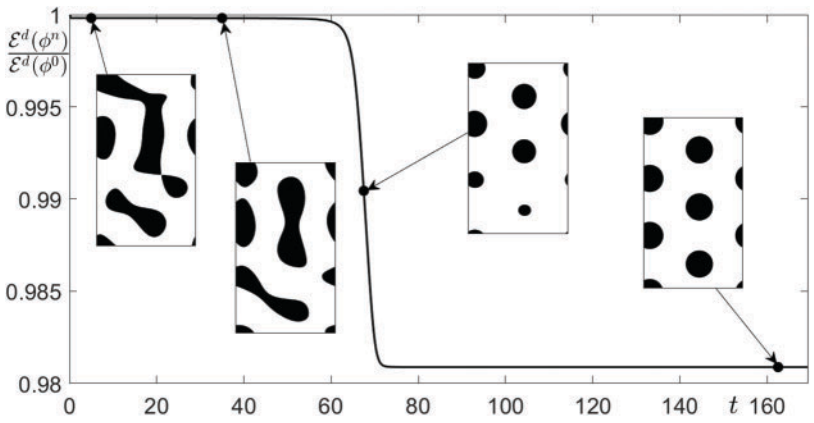

Figure 9: The discrete total energy with a snapshot of the numerical solutions

We observe the formation of a hexagonal pattern in the discrete equilibrium state and discrete total energy dissipation from numerical results. Chen et al. [56] presented a hydrodynamically-coupled phase-field model for diblock copolymer melts based on a conservative Allen–Cahn equation that preserves the volume fraction of the two monomers. In addition, the authors developed the linear and second-order time-marching method for the presented phase-field model. This method is easy to implement and can also be applied to a variety of phase-field models, such as CH equation for the diblock copolymer melts.

2.3 Alternating Direction Explicit

Yang et al. [57] developed an explicit FDM for the Ohta–Kawasaki model to describe microphase separation patterns in diblock copolymer melts. Their approach employs a Saul'yev-type scheme, which is grounded in a linearly stabilized convex splitting method, to achieve effective discretizations of the model equations. This method enhances the numerical stability of the simulations, allowing for more stable predictions of the complex behavior exhibited by diblock copolymer melts. The discrete domain is defined by using cell center points. The NCH Eqs. (1) and (2) are rewritten by applying the linear convex splitting-type scheme [58] as

$$\frac{\phi_{ij}^{n+1}-\phi_{ij}^{n}}{\Delta t}=\Delta\left[(\phi_{ij}^{n})^3-3\phi_{ij}^{n}\right]+2\Delta\phi_{ij}^{n+1}-\varepsilon^2\Delta^2\phi_{ij}^{n+1}-\alpha(\phi_{ij}^{n+1}-\bar{\phi}), \tag{23}$$

where

$$\Delta\phi_{ij}=\frac{\phi_{i-1,j}+\phi_{i+1,j}+\phi_{i,j-1}+\phi_{i,j+1}-4\phi_{ij}}{h^2} \text{ and } \Delta^2\phi_{ij}=\frac{\Delta\phi_{i-1,j}+\Delta\phi_{i+1,j}+\Delta\phi_{i,j-1}+\Delta\phi_{i,j+1}-4\Delta\phi_{ij}}{h^2}.$$

Then, we use the Saul'yev-type method [59]. There are a total of 8 cases considering the order of i and j, and whether i is increasing or decreasing, as well as whether j is increasing or decreasing. One of these cases is as follows, and the remaining 7 cases are derived similarly.

$$\text{For } j=1,2,\ldots,N_y, \quad \text{for } i=1,2,\ldots,N_x, \tag{24}$$

$$\begin{aligned}\frac{\phi_{ij}^{n+1}-\phi_{ij}^{n}}{\Delta t} &= \Delta[(\phi_{ij}^{n})^3-3\phi_{ij}^{n}]+\frac{2}{h^2}\left(\phi_{i-1,j}^{n+1}+\phi_{i+1,j}^{n}-2\phi_{ij}^{n}-2\phi_{ij}^{n+1}+\phi_{i,j-1}^{n+1}+\phi_{i,j+1}^{n}\right)\\ &-\frac{\varepsilon^2}{h^4}\left[\phi_{i-2,j}^{n+1}+\phi_{i+2,j}^{n}+\phi_{i,j-2}^{n+1}+\phi_{i,j+2}^{n}+2(\phi_{i-1,j-1}^{n+1}+\phi_{i-1,j+1}^{n}+\phi_{i+1,j-1}^{n+1}+\phi_{i+1,j+1}^{n})\right.\\ &\left.-8(\phi_{i-1,j}^{n+1}+\phi_{i+1,j}^{n}+\phi_{i,j-1}^{n+1}+\phi_{i,j+1}^{n})+10\phi_{ij}^{n}+10\phi_{ij}^{n+1}\right]-\alpha(\phi_{ij}^{n+1}-\bar{\phi}).\end{aligned} \tag{25}$$

We can simplify Eq. (25) as

$$\begin{aligned}\phi_{ij}^{n+1} &= \frac{1}{r}\left\{\frac{\phi_{ij}^{n}}{\Delta t}+\Delta[(\phi_{ij}^{n})^3-3\phi_{ij}^{n}]+\frac{2}{h^2}\left(\phi_{i-1,j}^{n+1}+\phi_{i+1,j}^{n}-2\phi_{ij}^{n}+\phi_{i,j-1}^{n+1}+\phi_{i,j+1}^{n}\right)\right.\\ &-\frac{\varepsilon^2}{h^4}\left[\phi_{i-2,j}^{n+1}+\phi_{i+2,j}^{n}+\phi_{i,j-2}^{n+1}+\phi_{i,j+2}^{n}+2(\phi_{i-1,j-1}^{n+1}+\phi_{i-1,j+1}^{n}+\phi_{i+1,j-1}^{n+1}+\phi_{i+1,j+1}^{n})\right.\\ &\left.\left.-8(\phi_{i-1,j}^{n+1}+\phi_{i+1,j}^{n}+\phi_{i,j-1}^{n+1}+\phi_{i,j+1}^{n})+10\phi_{ij}^{n}\right]+\alpha\bar{\phi}\right\},\end{aligned} \tag{26}$$

where $r = 1/\Delta t + 4/h^2 + 10\varepsilon^2/h^4 + \alpha$.

We consider the irregular domain $\hat{\Omega}$, which is depicted as the gray region in Fig. 10. The initial condition on the full domain $\Omega = (-2, 2) \times (-2, 2)$ is given by

$$\phi(x, y, 0) = \begin{cases}\bar{\phi} + 0.15\text{rand}(x, y) & \text{if } (x, y) \in \hat{\Omega},\\ -0.75 & \text{otherwise.}\end{cases}$$

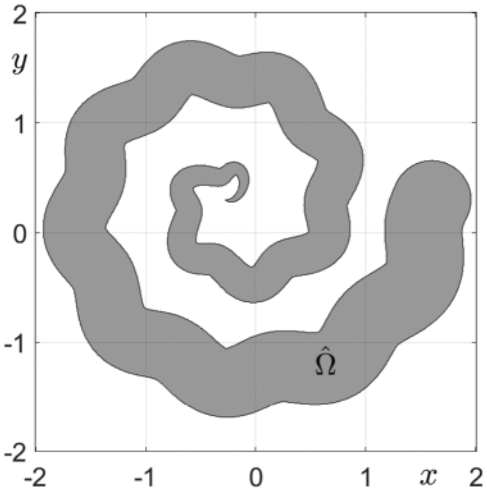

Figure 10: Schematic illustrations of the irregular domain $\hat{\Omega}$

For the numerical test, we used parameters $N_x = N_y = 800$, $\varepsilon = 0.01$, $\alpha = 800$, $\bar{\phi} = 0, \ -0.3$, and $\Delta t = h^2$. Fig. 11 displays the temporal evolution of the numerical solution for the NCH equation on the complex domain using the alternating direction explicit FDM for the phase-field equation.

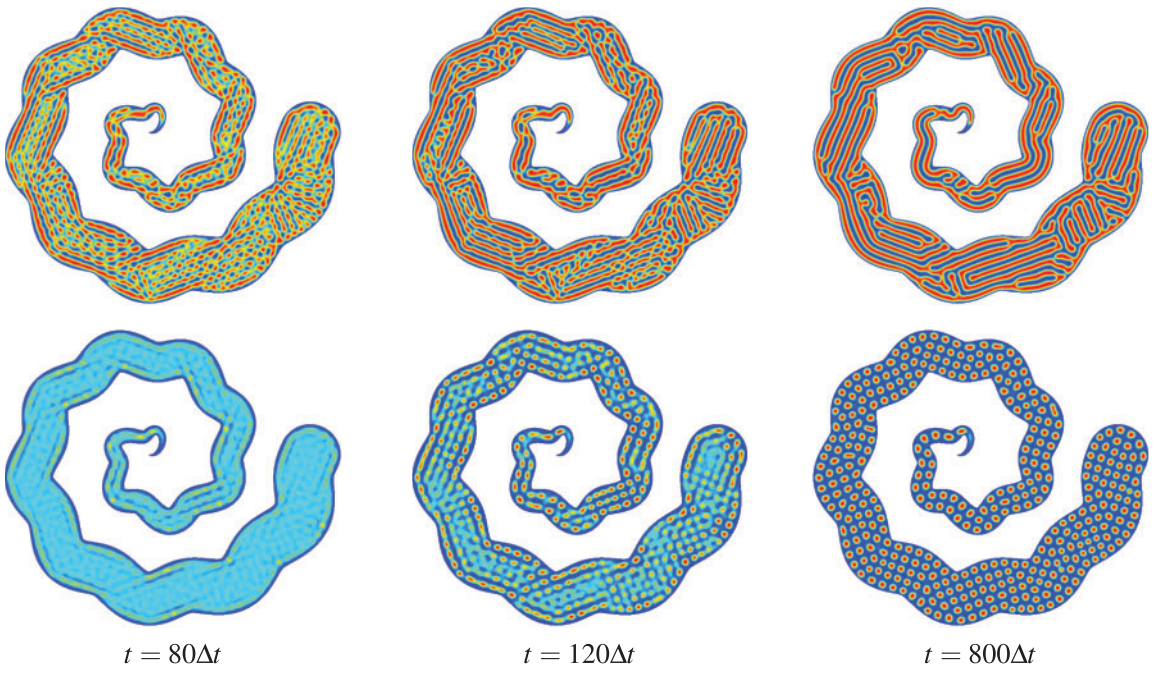

Figure 11: Pattern formations in irregular domain $\hat{\Omega}$. From the top to bottom, $\bar{\phi} = 0$ and -0.3

Next, we perform numerical simulations to investigate how different boundary conditions, such as Dirichlet and Neumann boundary conditions, influence the simulation results. The initial condition is given by $\phi(x, y, 0) = \text{rand}(x, y)$ on $\Omega = (-1, 1) \times (-1, 1)$. For zero Dirichlet boundary condition, the boundary values are set as $\phi_{-1,j} = \phi_{0,j} = \phi_{i,-1} = \phi_{i,0} = \phi_{N_x+1,j} = \phi_{N_x+2,j} = \phi_{i,N_y+1} = \phi_{i,N_y+2} = 0$ for $i = 1, 2, \ldots, N_x$, $j = 1, 2, \ldots, N_y$. For non-zero Dirichlet boundary condition, the boundary values are assigned as $\phi_{-1,j} = \phi_{0,j} = \phi_{i,-1} = \phi_{i,0} = \phi_{N_x+1,j} = \phi_{N_x+2,j} = \phi_{i,N_y+1} = \phi_{i,N_y+2} = -0.7$ for $i = 1, 2, \ldots, N_x$, $j = 1, 2, \ldots, N_y$. For Neumann boundary condition, the boundary values are set as $\phi_{-1,j} = \phi_{2,j}$, $\phi_{0,j} = \phi_{1,j}$, $\phi_{N_x+1,j} = \phi_{N_x,j}$, and $\phi_{N_x+2,j} = \phi_{N_x-1,j}$ for $j = 1, 2, \ldots, N_y$, $\phi_{i,-1} = \phi_{i,2}$, $\phi_{i,0} = \phi_{i,1}$, $\phi_{i,N_x+1} = \phi_{i,N_x}$, and $\phi_{i,N_x+2} = \phi_{i,N_x-1}$ for $i = 1, 2, \ldots, N_x$.

Fig. 12 shows the numerical solutions obtained under different boundary conditions. From top to bottom, the results correspond to $\bar{\phi} = 0$ and $\bar{\phi} = -0.3$. The numerical solutions using Dirichlet boundary conditions with values of 0 and -0.7 are shown in Fig. 12a,b, respectively. The solution using the Neumann boundary condition is presented in Fig. 12c. We observed that the Dirichlet boundary condition enforces fixed values near the boundaries, influencing pattern formation. The non-zero Dirichlet boundary condition with a boundary value of -0.7 produces a different pattern near the boundary compared to the zero Dirichlet boundary condition. In contrast, the Neumann boundary condition maintains continuity at the boundaries, resulting in smoother and more regular patterns.

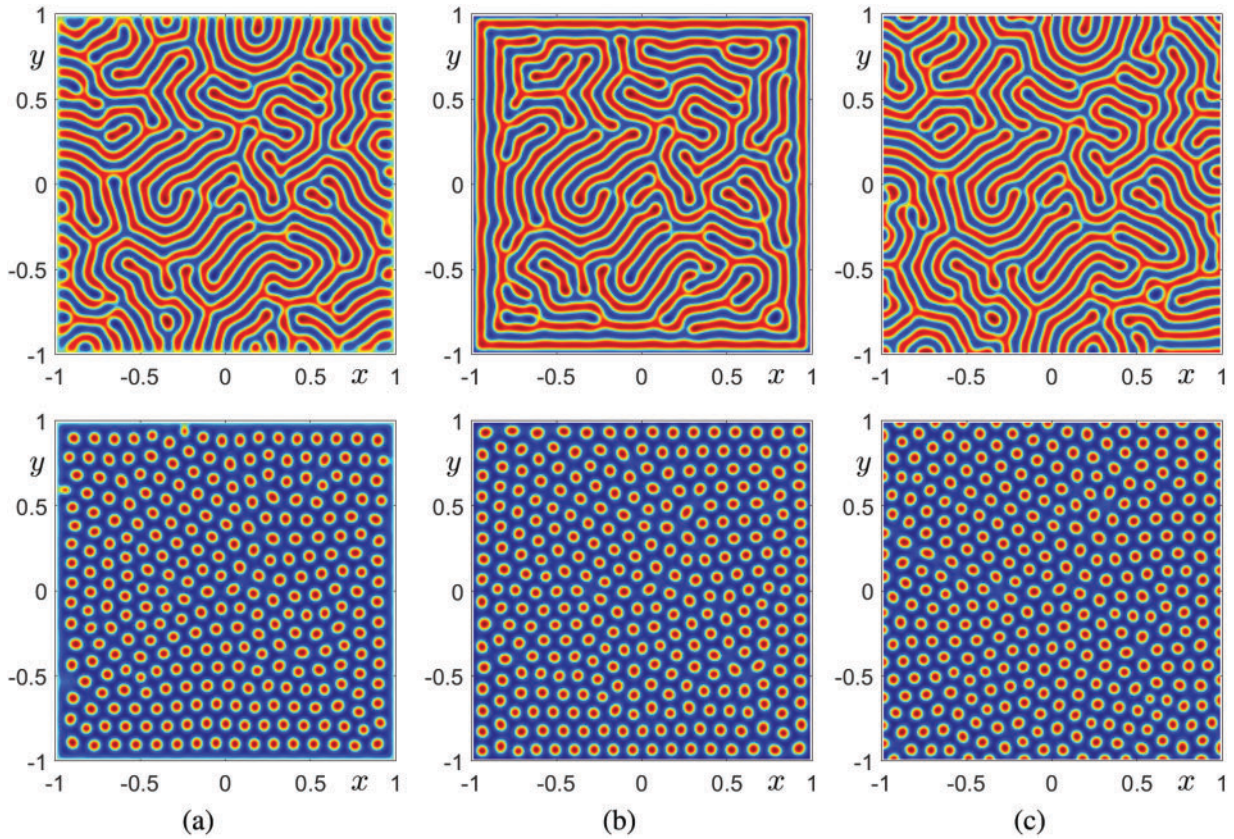

Figure 12: Numerical solutions at time $t = 1000\Delta t$ with different boundary conditions. (a) zero Dirichlet, (b) non-zero (−0.7) Dirichlet, and (c) Neumann boundary conditions. From the top to bottom, $\bar{\phi} = 0$ and −0.3

2.4 Invariant Energy Quadratization Approach

The invariant energy quadratization (IEQ) method is a numerical method designed to ensure energy stability when solving gradient flow problems. Originally proposed by Yang [60], the IEQ method transforms nonlinear partial differential equations into a form that allows for constructing energy-stable time-marching schemes. We simply describe an IEQ approach for the NCH equation. The auxiliary variable is defined as $q(\phi) = \sqrt{F(\phi) + C}$. Then, the total free energy is rewritten as

$$\mathscr{E}(q,\phi) = \int_\Omega \left(\frac{\varepsilon^2}{2}|\nabla\phi|^2 + \frac{\alpha}{2}|\nabla\omega|^2 + q^2 \right) d\mathbf{x} - C.$$

We get

$$\frac{\partial\phi}{\partial t} = \Delta\mu, \tag{27}$$

$$\mu = qH(\phi) - \varepsilon^2\Delta\phi + \alpha\omega, \tag{28}$$

$$\frac{dq}{dt} = \frac{1}{2}H(\phi)\frac{\partial\phi}{\partial t}, \tag{29}$$

where

$$H(\phi) = \frac{F'(\phi)}{\sqrt{F(\phi) + C}}.$$

Therefore, we can obtain the energy dissipation law of the system (27)–(29) by taking the L^2 inner product of Eqs. (27)–(29) with $-\mu$, ϕ_t, and $-2q$, respectively.

$$\frac{d}{dt}\mathscr{E}(q, \phi) = -\|\nabla\mu\|^2 \leq 0.$$

The first-order time discretization IEQ method for the system (27)–(29) is defined by

$$\frac{\phi^{n+1} - \phi^n}{\Delta t} = \Delta\mu^{n+1}$$
$$\mu^{n+1} = Sq^{n+1}H^n - \varepsilon^2\Delta\phi^{n+1} + \omega^{n+1}$$
$$q^{n+1} - q^n == \frac{1}{2}H^n(\phi^{n+1} - \phi^n).$$

The solution algorithms for the CH equation using the IEQ scheme is studied by Chen et al. [61], which are unconditionally stable. Two numerical methods, each first-order and second-order are reported. Numerical simulations showed that a large time step can be adopted while maintaining the energy decrease, therefore verifying the applicability of the proposed method.

2.5 Scalar Auxiliary Variable Approach

The SAV scheme was originally proposed by Shen et al. [62] and based on the IEQ approach, constructs energy-stable and efficient time discretization methods for gradient flows. The SAV scheme is applicable to different gradient flows and can be extended to higher-order by applying the backward differentiation formula (BDF) and Adam–Bashforth methods. We describe an SAV scheme for the NCH equation. The scalar auxiliary variable $r(t)$ is defined by

$$r(t) = \sqrt{\int_\Omega F(\phi(\mathbf{x}, t))d\mathbf{x} + C},$$

where C is a non-negative constant, which guarantees the value beneath the square root is not zero. Thus, we have

$$\mathscr{E}(r, \phi) = \int_\Omega \left(\frac{\varepsilon^2}{2}|\nabla\phi|^2 + \frac{\alpha}{2}|\nabla\omega|^2\right)d\mathbf{x} + r^2 - C.$$

Hence, we get

$$\frac{\partial\phi(\mathbf{x}, t)}{\partial t} = \Delta\mu(\mathbf{x}, t), \tag{30}$$
$$\mu(\mathbf{x}, t) = r(t)H(\phi(\mathbf{x}, t)) - \varepsilon^2\Delta\phi(\mathbf{x}, t) + \alpha\omega(\mathbf{x}, t), \tag{31}$$
$$\frac{dr(t)}{dt} = \frac{1}{2}\int_\Omega H(\phi(\mathbf{x}, t))\frac{\partial\phi(\mathbf{x}, t)}{\partial t}d\mathbf{x}, \tag{32}$$

where

$$H(\phi) = \frac{F'(\phi)}{\sqrt{\int_\Omega F(\phi)d\mathbf{x} + C}}.$$

We take the L^2 inner product of Eqs. (30) and (31) with $-\mu$ and ϕ_t, respectively, and multiply Eq. (32) by $2r$. Next, we perform integration by parts for the obtained system, then obtain the time derivative for ω and take L^2 inner products with ω, and summing all the equations to get the total free energy dissipation law.

$$\frac{d}{dt}\mathscr{E}(r,\phi) = -\|\nabla\mu\|^2 \le 0.$$

Zhang et al. [63] developed the stabilized SAV scheme for solving the CH phase field equation for diblock copolymers. The authors applied BDF2 to the SAV method for the NCH equation. We discretize the system (30)–(32) with respect to time.

$$\frac{3\phi^{n+1} - 4\phi^n + \phi^{n-1}}{2\Delta t} = \Delta\mu^{n+1}, \tag{33}$$

$$\mu^{n+1} = r^{n+1}H^* - \varepsilon^2\Delta\phi^{n+1} + \alpha\omega^{n+1} + S(\phi^{n+1} - \phi^*), \tag{34}$$

$$3r^{n+1} - 4r^n + r^{n-1} = \frac{1}{2}\int_\Omega H^*(3\phi^{n+1} - 4\phi^n + \phi^{n-1})d\mathbf{x}, \tag{35}$$

where S is a positive stabilizing parameter, $\phi^* = 2\phi^n - \phi^{n-1}$, and $H^* = H(\phi^*)$. To solved the Eqs. (33)–(35), we need values of ϕ^1, μ^1, and r^1. Thus, calculated the Eqs. (30)–(32) using the first-order method based on the backward Euler method as

$$\frac{\phi^1 - \phi^0}{\Delta t} = \Delta\mu^1,$$

$$\mu^1 = r^1H^0 - \varepsilon^2\Delta\phi^{n+1} + \alpha\omega^1 + S(\phi^1 - \phi^0),$$

$$r^1 - r^0 = \frac{1}{2}\int_\Omega H^0(\phi^1 - \phi^0)d\mathbf{x},$$

where ϕ^0, μ^0, and r^0 are initial conditions.

Theorem 1. *Suppose that ϕ^n, r^n, ϕ^{n-1}, and r^{n-1} are given. The discrete system (33)–(35) is unconditionally energy stable which satisfies the discrete energy dissipation law.*

$$\mathscr{E}^{n+1} - \mathscr{E}^n \le -\Delta t\|\nabla\mu^{n+1}\|^2 \le 0,$$

where

$$\mathscr{E}^{n+1} = \varepsilon^2\frac{\|\nabla\phi^{n+1}\|^2 + \|2\nabla\phi^{n+1} - \nabla\phi^n\|^2}{4} + \alpha\frac{\|\nabla\omega^{n+1}\|^2 + \|2\nabla\omega^{n+1} - \nabla\omega^n\|^2}{4} + \frac{(r^{n+1})^2 + (2r^{n+1} - r^n)^2}{2} + S\frac{\|\phi^{n+1} - \phi^n\|^2}{2}.$$

Proof. We take the L^2 inner product of (33) and $-2\Delta t\mu^{n+1}$.

$$-\left(3\phi^{n+1} - 4\phi^n + \phi^{n-1}, \mu^{n+1}\right) = 2\Delta t\|\nabla\mu^{n+1}\|^2.$$

Then, we take the L^2 inner product of (34) and $3\phi^{n+1} - 4\phi^n + \phi^{n-1}$, and using integration by parts.

$$\begin{aligned}\left(\mu^{n+1}, 3\phi^{n+1} - 4\phi^n + \phi^{n-1}\right) = r^{n+1}\left(H^*, 3\phi^{n+1} - 4\phi^n + \phi^{n-1}\right) + \varepsilon^2\left(\nabla\phi^{n+1}, 3\nabla\phi^{n+1} - 4\nabla\phi^n + \nabla\phi^{n-1}\right)\\ + S\left(\phi^{n+1} - 2\phi^n + \phi^{n-1}, 3\phi^{n+1} - 4\phi^n + \phi^{n-1}\right)\\ + \alpha\left(\omega^{n+1}, 3\phi^{n+1} - 4\phi^n + \phi^{n-1}\right).\end{aligned} \tag{36}$$

From $-\Delta\omega = \phi - \bar{\phi}$, we can derive following equation.

$$-\Delta\left(3\omega^{n+1} - 4\omega^n + \omega^{n-1}\right) = 3\phi^{n+1} - 4\phi^n + \phi^{n-1} - \left(3\bar{\phi}^{n+1} - 4\bar{\phi}^n + \bar{\phi}^{n-1}\right). \tag{37}$$

Since $\int_\Omega \omega^{n+1} d\mathbf{x} = 0$, we can obtain following equation by taking the L^2 inner product of (37) with $\alpha\omega^{n+1}$.

$$\alpha\left(3\nabla\omega^{n+1} - 4\nabla\omega^n + \nabla\omega^{n-1}, \nabla\omega^{n+1}\right) = \alpha\left(3\phi^{n+1} - 4\phi^n + \phi^{n-1}, \omega^{n+1}\right). \tag{38}$$

By multiplying (35) with $-2r^{n+1}$, we obtain the equation as

$$-2\left(3r^{n+1} - 4r^n + r^{n-1}\right)r^{n+1} = -r^{n+1}\int_\Omega H^*\left(3\phi^{n+1} - 4\phi^n + \phi^{n-1}\right) d\mathbf{x}. \tag{39}$$

We consider two identities follows

$$\begin{aligned}2x(3x - 4y + z) &= x^2 + (2x - y)^2 - y^2 - y^2 - (2y - z)^2 + (x - 2y + z)^2,\\ (3x - 4y + z)(x - 2y + z) &= (x - y)^2 - (y - z)^2 + 2(x - 2y + z)^2.\end{aligned}$$

Next, we combine the Eqs. (36)–(39) and by using the above two identities to get

$$\begin{aligned}&\frac{\varepsilon^2}{2}\left(\|\nabla\phi^{n+1}\|^2 + \|2\nabla\phi^{n+1} - \nabla\phi^n\|^2\right) + \frac{\alpha}{2}\left(\|\nabla\omega^{n+1}\|^2 + \|2\nabla\omega^{n+1} - \nabla\omega^n\|^2\right)\\ &+ \left(r^{n+1}\right)^2 + \left(2r^{n+1} - r^n\right)^2 + S\|\phi^{n+1} - \phi^n\|^2\\ &- \frac{\varepsilon^2}{2}\left(\|\nabla\phi^n\|^2 + \|2\nabla\phi^n - \nabla\phi^{n-1}\|^2\right) - \frac{\alpha}{2}\left(\|\nabla\omega^n\|^2 + \|2\nabla\omega^n - \nabla\omega^{n-1}\|^2\right)\\ &- \left(r^n\right)^2 - \left(2r^n - r^{n-1}\right)^2 - S\|\phi^n - \phi^{n-1}\|^2 + \frac{\varepsilon^2}{2}\|\nabla\phi^{n+1} - 2\nabla\phi^n + \nabla\phi^{n-1}\|^2\\ &+ \frac{\alpha}{2}\|\nabla\omega^{n+1} - 2\nabla\omega^n + \nabla\omega^{n-1}\|^2 + \left(r^{n+1} - 2r^n + r^{n-1}\right)^2 + 2S\|\phi^{n+1} - 2\phi^n + \phi^{n+1}\|^2\\ &= -2\Delta t\|\nabla\mu^{n+1}\|^2.\end{aligned}$$

We can rewrite the above equation using the definition of total free energy as

$$\begin{aligned}\mathscr{E}^{n+1} - \mathscr{E}^n = -\Delta t\|\nabla\mu^{n+1}\|^2 - \frac{\varepsilon^2}{4}\|\nabla\phi^{n+1} - 2\nabla\phi^n + \nabla\phi^{n-1}\|^2 - \frac{\alpha}{4}\|\nabla\omega^{n+1} - 2\nabla\omega^n + \nabla\omega^{n-1}\|^2\\ - \frac{1}{2}\left(r^{n+1} - 2r^n + r^{n-1}\right)^2 - S\|\phi^{n+1} - 2\phi^n + \phi^{n+1}\|^2.\end{aligned}$$

In the right-hand terms of the above equation, the sum of all terms except $-\Delta t\|\nabla\mu^{n+1}\|^2$ is negative, thus we obtain the following inequality.

$$\mathscr{E}^{n+1} - \mathscr{E}^n \le -\Delta t\|\nabla\mu^{n+1}\|^2.$$

Thus, the discrete system (33)–(35) satisfies the discrete energy emission law. □

Zhang et al. [64] expanded a magnetic-coupled diblock copolymer system by introducing a magnetic field in the CH equation for diblock copolymers. The authors developed the second-order time marching method using the stabilized SAV scheme to solve model. Wu et al. [65] developed a method with temporally second-order accuracy and unconditional energy stability based on the SAV approach scheme for a coupled CH system to simulate phase separation in the homopolymer and copolymer mixtures. In addition, the authors used the Fourier spectral method for space to minimize errors in space. Huang et al. [66] establish the error estimates of the SAV scheme for the coupled CH equation in the diblock copolymer. The numerical method is based on the SAV approach for time and the Fourier spectral method for space. Li et al. [67] applied the IEQ method to simulate anisotropic dendritic crystal growth with an azimuthal field, developing a second-order unconditionally energy-stable numerical scheme validated through simulations of complex growth processes. Jiang et al. [68] employed the SAV method to study fluid-surfactant systems on curved surfaces, demonstrating the precision and efficiency of their second-order, unconditionally energy-stable scheme. Lai et al. [69] extended the SAV method to analyze connected regions in digital models, proposing a stable and efficient algorithm for complex structure analysis. In [70], the authors proposed a conservative Allen–Cahn equation for diblock copolymers. They developed a numerical method based on the stabilized SAV scheme to solve the developed model. Through numerical tests, they validated the effectiveness of the new model by comparing it with the CH diblock copolymer model.

3 Applications of the Phase-Field Diblock Copolymer Model

The phase-field model for microphase separation patterns in diblock copolymer melts is widely applicable to various applications. Its capability to describe complex behaviors and microstructural patterns during phase separation makes it a valuable tool in materials science and polymer research. We present a detailed discussion on several examples, including fingerprint image restoration and 3D printing. Beyond these examples, the NCH equation has been widely applied in various fields, particularly in biology and materials science. In biology, the Green's function$G$ from Eq. (4) plays a critical role in modeling cancer cell invasion [71] and solid tumor growth [72]. In materials science, the NCH equation has been particularly successful in describing diverse phenomena. Notable examples include mesoscopic models of particle dynamics for pattern formation [73] and phase transitions [74]. These examples highlight the versatility of the NCH equation across multiple disciplines.

3.1 Fingerprint Image Restoration

Lee et al. [75] presented a semi-automatic fingerprint image restoration algorithm using the NCH equation for the damaged fingerprint images. The developed fingerprint image restoration algorithm is based on the alternating direction explicit scheme [57]. Let Ω be the global domain for the given fingerprint image and let Ω_k be the damaged area of the fingerprint image, where k is the number of the damaged areas. Fig. 13 shows the global domain for the given fingerprint image, the damaged area, and the computational discrete domain for the damaged area. To restoration of the damaged fingerprint, we solved the NCH equation on the Ω_1 with Dirichlet boundary conditions. The initial conditions within the computational domain Ω_1 are obtained from a damaged fingerprint. Additionally, the points in the neighborhood outside of the damaged area for the computation are derived from the given fingerprint image and are used as fixed values. This is illustrated in Fig. 13b, where the points computed within the domain are represented as unfilled circles, while the points outside Ω_1 with fixed, non-computed values are represented as filled circles.

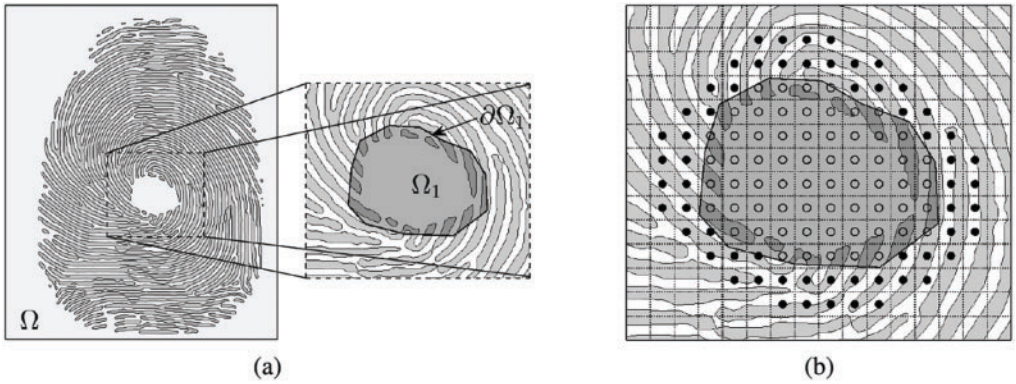

Figure 13: Schematic illustrations of (a) the global domain Ω_1 for the damaged fingerprint image and (b) the discrete domain Ω_1^d

We used the semi-automatic fingerprint image restoration algorithm based on the NCH equation to restore the damaged fingerprints. The main idea of the algorithm proposed by the authors is to find a spatial step size h, which is appropriately tuned to a given fingerprint data. This determines h using fixed parameters α, ε, and Δt, based on pattern information close to the corrupted region. For more details, please refer to [75]. Fig. 14 shows the given damaged fingerprint and the restored fingerprint using the developed algorithm [75]. Here, we used the parameters $\alpha = 0.1$, $\Delta t = 0.1$, and $\varepsilon = 1.2$. Fig. 14a shows the initial condition, where the region inside the black line represents the damaged area assigned with a value of 0. The red line indicates the 1D domain where pattern information near the computational domain was analyzed to determine the appropriate spatial step size. Fig. 14b,c shows snapshots of the numerical solution at $t = 100\Delta t$ and at the numerical equilibrium state, which is achieved at $t = 29576\Delta t$. The numerical solutions obtained using the semi-automatic fingerprint image restoration algorithm effectively reconstructed the damaged region by employing the boundary values and an appropriately chosen spatial step size h.

Figure 14: Numerical solution of the NCH equation using the semi-automatic fingerprint image restoration algorithm at times $t = 0, 100\Delta t$, and $29576\Delta t$

3.2 3D Printing

Lee et al. [76] proposed a numerical method to generate a porous structure of arbitrary shape for 3D printing. The numerical method is based on the Fourier spectral method [55]. We used parameter $N_x = N_y = 100$, $N_z = 200$, $\varepsilon = 2h/(2\sqrt{2}\tanh^{-1}(0.9))$, $\Delta t = 10h^2$, and $\alpha = 100, 700, 1500$. The initial condition on $\Omega = (0,1) \times (0,1) \times (0,2)$ is given by $\phi(x, y, 0) = -0.3 + 0.1\text{rand}(x, y)$. Fig. 15 displays the computational solutions solved by using the numerical algorithm [76] with $\alpha = 100$, 700 and 1500 at $t = 300\Delta t$.

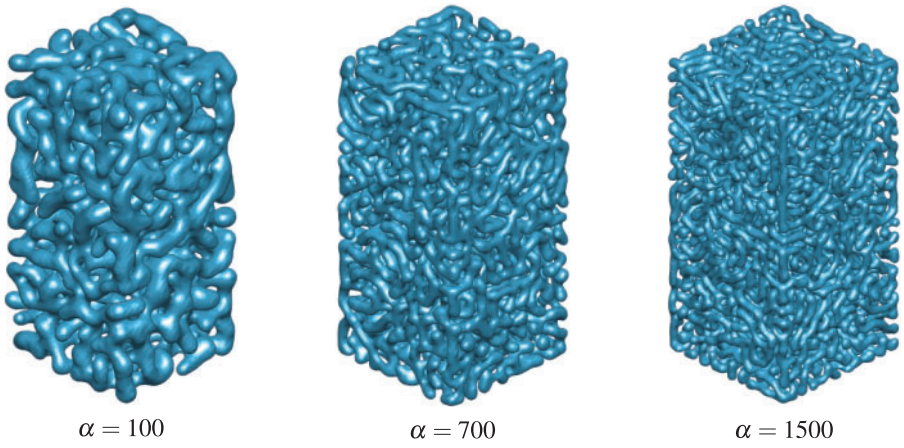

Figure 15: The 0-level isosurfaces of the numerical solutions for $\alpha = 100$, 700, and 1500

Various distance functions can be utilized to generate porous structures within other solid geometries that are not cubes. Please refer to [76]. The generation of porous structures has the advantage of controlling the shape of the porosity through the space-dependent average concentration function $\bar{\phi}$, and the algorithm is simple to implement.

Yoon et al. [77] presented a numerical algorithm to make uniformly distributed circular porous patterns on curved surfaces for 3D printing structures in 3D space using the computational method for the NCH equation [24]. The authors defined a narrow band domain including the surface to efficiently and simply solve the NCH equation, enabling the generation of circular porous patterns on the surface. Xia et al. [78] applied an unconditionally energy-stable numerical scheme to analyze the Swift–Hohenberg equation on arbitrary surfaces, achieving stable, second-order accurate results. Li et al. [79] developed a direct discretization technique to solve multicomponent CH systems on surfaces, yielding precise and stable solutions. Additionally, Xia et al. [80] introduced an unconditionally energy-stable phase-field approach for simulating binary thermal fluids on arbitrary surfaces with high accuracy. For numerical simulation, we used parameters $N_x = N_y = N_z = 152$, $\varepsilon = 4h/(2\sqrt{2}\tanh^{-1}(0.9))$, $\Delta t = 100h$, and $\alpha = 100,400,700$. The initial condition on $\Omega = (-1,1) \times (-1,1) \times (-1,1)$ is defined by $\phi(x, y, 0) = -0.3 + 0.2\text{rand}(x, y)$. Fig. 16 shows the computational solutions ϕ and the corresponding isosurface with $\phi = -0.3$ at time $t = 300\Delta t$. Fig. 16a shows the scalar field ϕ computed on a spherical surface, representing uniformly distributed circular porous patterns. As the value of α increases, the number of pores grows significantly, while the size of individual pores decreases. Fig. 16b presents the isosurface extracted at the level $\phi = -0.3$, highlighting the three-dimensional porous structures. For $\alpha = 100$, the pores are relatively large and fewer in number. At $\alpha = 400$, the pore size decreases while their number increases. When $\alpha = 700$, the pores become even smaller and denser, forming a finer and more intricate pattern. These results demonstrate that the proposed numerical method can precisely control the size and distribution of porous patterns by adjusting the parameter α. This

capability is particularly useful for applications in 3D printing, where such porous structures can be employed in fields like tissue engineering, biomaterials, and lightweight structural design.

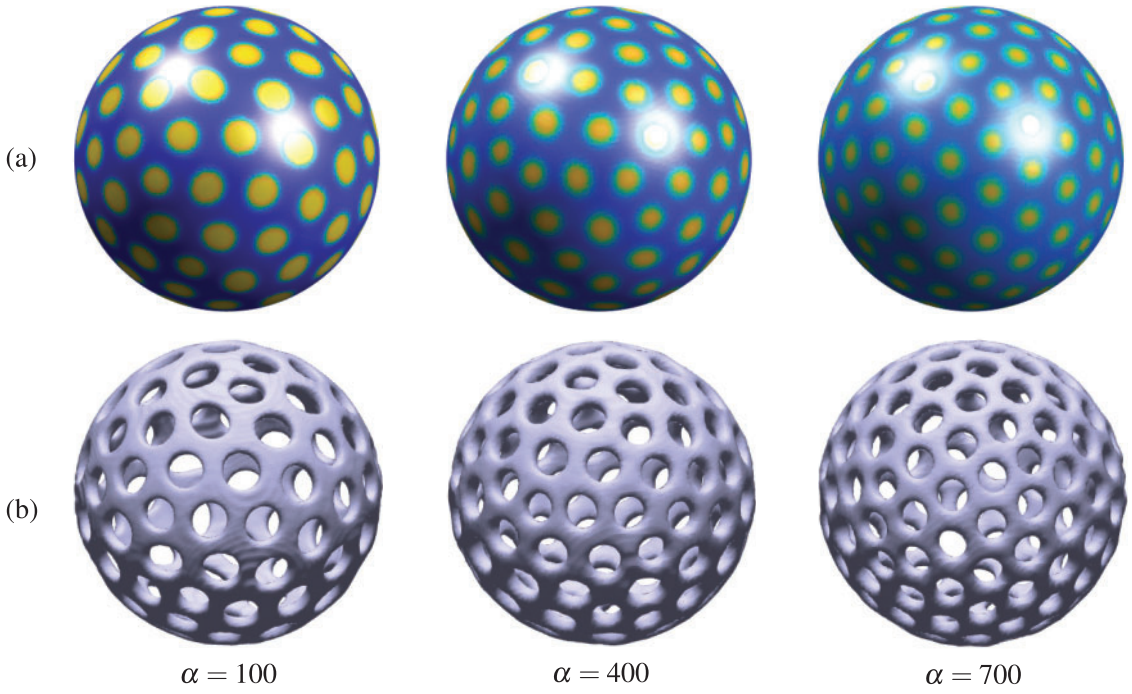

Figure 16: (a) Numerical solutions on the surface and (b) isosurfaces at $\phi = -0.3$ of the numerical solutions. From left to right, α = 100, 400, 700

4 Conclusion

In this review paper, we extensively presented various numerical methods that model the phase separation dynamics of diblock copolymer melts through the phase-field model. Many applications adopted the diblock copolymer system to create and simulate the movement of phase boundaries of nanoscale complex structures. We examined five state-of-the-art numerical methods that solve the nonlocal Cahn–Hilliard equation. The finite difference method was simple to implement and broadly applicable. However, it had limitations in complex domains. On the other hand, the Fourier spectral method is suitable for solving models in complex domains, but is limited to specific boundary conditions and cell-centred grids. The alternating direction explicit method allowed more stable predictions on complex domains, but had to handle the error from splitting the governing equation. The invariant energy quadratization method proposed by Yang and the scalar auxiliary variable approach by Shen et al. showed their strength in energy stability. Furthermore, we introduce recent applications of the phase-field model such as Fingerprint image restoration and 3D printing to illustrate its versatility in different fields. Overall, this analysis serves as a valuable resource for researchers seeking to understand and apply numerical methods in the study of diblock copolymer melts.

Acknowledgement: The corresponding author (Junseok Kim) and coauthors express their gratitude to the reviewers for their valuable comments, which have enhanced the quality of this manuscript.

Funding Statement: The authors received no specific funding for this study.

Author Contributions: The authors confirm contribution to the paper as follows: study conception and design: Youngjin Hwang, Junseok Kim; methodology: Youngjin Hwang, Junseok Kim; software: Youngjin Hwang, Seungyoon

Kang; visualization: Youngjin Hwang; formal analysis: Youngjin Hwang; validation: Youngjin Hwang, Seungyoon Kang; investigation: Youngjin Hwang, Seungyoon Kang; draft manuscript preparation: Youngjin Hwang, Seungyoon Kang, Junseok Kim; project administration: Junseok Kim; supervision: Junseok Kim; funding acquisition: Junseok Kim. All authors reviewed the results and approved the final version of the manuscript.

Availability of Data and Materials: The data that support the findings of this study are available from the corresponding author, Junseok Kim, upon reasonable request.

Ethics Approval: Not applicable.

Conflicts of Interest: The authors declare no conflicts of interest to report regarding the present study.

References

1. Ohta T, Kawasaki K. Equilibrium morphology of block copolymer melts. Macromolecules. 1986;19(10):2621–32. doi:10.1021/ma00164a028.
2. Farrell PE, Pearson JW. A preconditioner for the Ohta-Kawasaki equation. SIAM J Matrix Analy Appl. 2017;38(1):217–25. doi:10.1137/16M1065483.
3. Matsen MW, Schick M. Stable and unstable phases of a diblock copolymer melt. Phys Rev Lett. 1994;72(16):2660. doi:10.1103/PhysRevLett.72.2660.
4. Fish J, Wagner GJ, Keten S. Mesoscopic and multiscale modelling in materials. Nature Mat. 2021;20(6):774–86. doi:10.1038/s41563-020-00913-0.
5. Chen LQ. Phase-field models for microstructure evolution. Ann Rev Mat Res. 2002;32(1):113–40. doi:10.1146/annurev.matsci.32.112001.132041.
6. Van Den Berg JB, Williams J. Rigorously computing symmetric stationary states of the Ohta-Kawasaki problem in three dimensions. SIAM J Mathem Anal. 2019;51(1):131–58. doi:10.1137/17M1155624.
7. Barros GF, Côrtes AM, Coutinho AL. Finite element solution of nonlocal Cahn-Hilliard equations with feedback control time step size adaptivity. Int J Num Meth Eng. 2021;122(18):5028–52. doi:10.1002/nme.6755.
8. Cao L, Ghattas O, Oden JT. A globally convergent modified newton method for the direct minimization of the ohta-kawasaki energy with application to the directed self-assembly of diblock copolymers. SIAM J Sci Comput. 2022;44(1):B51–79. doi:10.1137/20M1378119.
9. Singh PK, Cao L, Tan J, Faghihi D. A nonlocal theory of heat transfer and micro-phase separation of nanostructured copolymers. Int J Heat Mass Transf. 2023;215(1):124474. doi:10.1016/j.ijheatmasstransfer.2023.124474.
10. Yasen W, Dong R, Aini A, Zhu X. Recent advances in supramolecular block copolymers for biomedical applications. J Mat Chem B. 2020;8(36):8219–31. doi:10.1039/D0TB01492C.
11. Iqbal MJ, Soomro I, Razzaq MA, Martinez EO, Martinez ZLV, Ashraf I. Investigation of structural frustration in symmetric diblock copolymers confined in polar discs through cell dynamic simulation. Sci Rep. 2024;14(1):25916. doi:10.1038/s41598-024-76213-3.
12. Feng J, Ruckenstein E. Self-assembling of hydrophobic-hydrophilic copolymers in hydrophobic nanocylindrical tubes: formation of channels. J Chem Phys. 2008;128(7):074903. doi:10.1063/1.2831510.
13. Weyersberg A, Vilgis TA. Phase transitions in diblock copolymers: theory and Monte Carlo simulations. Phys Rev E. 1993;48(1):377. doi:10.1103/PhysRevE.48.377.
14. Dreyer O, Ibbeken G, Schneider L, Blagojevic N, Radjabian M, Abetz V, et al. Simulation of solvent evaporation from a diblock copolymer film: orientation of the cylindrical mesophase. Macromolecules. 2022;55(17):7564–82. doi:10.1021/acs.macromol.2c00612.
15. Gee RH, Lacevic N, Fried LE. Atomistic simulations of spinodal phase separation preceding polymer crystallization. Nature Mat. 2006;5(1):39–43. doi:10.1038/nmat1543.
16. Leibler L. Theory of microphase separation in block copolymers. Macromolecules. 1980;13(6):1602–17. doi:10.1021/ma60078a047.
17. Xu W, Jiang K, Zhang P, Shi AC. A strategy to explore stable and metastable ordered phases of block copolymers. J Phy Chem B. 2013;117(17):5296–305. doi:10.1021/jp309862b.

18. Pezzutti AD, Hernández H. Unconditionally stable algorithm for copolymer and copolymer-solvent systems. Pap Phy. 2020;12:120001. doi:10.4279/pip.120001.
19. Kravchenko VS, Abetz V, Potemkin II. Self-assembly of gradient copolymers in a selective solvent. New structures and comparison with diblock and statistical copolymers. Polymer. 2021;235:124288. doi:10.1016/j.polymer.2021.124288.
20. Chen T, Zhang Y, Xiao S, Yao D, Jiang W, Liang H. Catalytic assembly of symmetric diblock copolymers in a thin film: a dissipative particle dynamics simulation study. Phy Chem Chem Phy. 2023;25(14):9779–84. doi:10.1039/D3CP00447C.
21. Tomiyoshi Y, Oya Y, Kawakatsu T, Okabe T. Reaction-induced morphological transitions in a blend of diblock copolymers and reactive monomers: dissipative particle dynamics simulation. Soft Matter. 2024;20(1):124–32. doi:10.1039/D3SM00959A.
22. Jeong D, Choi Y, Kim J. Numerical investigation of local defectiveness control of diblock copolymer patterns. Conden Matter Phy. 2016;19(3):33001. doi:10.5488/CMP.19.33001.
23. Yang J. Linear energy-stable method with correction technique for the Ohta-Kawasaki–Navier-Stokes model of incompressible diblock copolymer melt. Commun Nonlinear Sci Numer Simul. 2024;131(1):101906 . doi:10.1016/j.cnsns.2024.107835.
24. Jeong D, Kim J. Microphase separation patterns in diblock copolymers on curved surfaces using a nonlocal Cahn-Hilliard equation. Eur Phy J E. 2015;38(11):1–7. doi:10.1140/epje/i2015-15117-1.
25. Muramatsu M, Yashiro K, Kawada T, Terada K. Simulation of ferroelastic phase formation using phase-field model. Int J Mech Sci. 2018;146:462–74. doi:10.1016/j.ijmecsci.2017.12.027.
26. Momeni K, Ji Y, Wang Y, Paul S, Neshani S, Yilmaz DE, et al. Multiscale computational understanding and growth of 2D materials: a review. NPJ Comp Mater. 2020;6(1):22. doi:10.1038/s41524-020-0280-2.
27. Endo K, Matsuda Y, Tanaka S, Muramatsu M. A phase-field model by an Ising machine and its application to the phase-separation structure of a diblock polymer. Sci Rep. 2022;12(1):10794. doi:10.1038/s41598-022-14735-4.
28. Shen X, Wang Q. Thermodynamically consistent algorithms for models of diblock copolymer solutions interacting with electric and magnetic fields. J Sci Comput. 2021;88(2):43. doi:10.1007/s10915-021-01470-7.
29. Adibi T, Ahmed SF, Razavi SE, Adibi O, Badruddin IA, Javed S. Impact of artificial compressibility on the numerical solution of incompressible nanofluid flow. Comput, Mat Cont. 2023;74(3):5123–39. doi:10.32604/cmc.2023.034008.
30. Song X, Xia Q, Kim J, Li Y. An unconditional energy stable data assimilation scheme for Navier-Stokes–Cahn-Hilliard equations with local discretized observed data. Comput Math Appl. 2024;164(10):21–33. doi:10.1016/j.camwa.2024.03.018.
31. Song X, Xia B, Li Y. An efficient data assimilation based unconditionally stable scheme for Cahn-Hilliard equation. Comput Appl Math. 2024;43(3):121. doi:10.1007/s40314-024-02632-7.
32. Martínez Agustín F, Ruiz Salgado S, Zenteno Mateo B, Rubio E, Morales M. 3D pattern formation from coupled Cahn-Hilliard and Swift-Hohenberg equations: morphological phases transitions of polymers, bock and diblock copolymers. Comput Mater Sci. 2022;210(5):111431. doi:10.1016/j.commatsci.2022.111431.
33. Barua AK, Chew R, Li S, Lowengrub J, Münch A, Wagner B. Sharp-interface problem of the Ohta-Kawasaki model for symmetric diblock copolymers. J Comput Phys. 2023;481(10):112032. doi:10.1016/j.jcp.2023.112032.
34. Meng X, Cheng A, Liu Z. The high-order exponential semi-implicit scalar auxiliary variable approach for the general nonlocal Cahn-Hilliard equation. Commun Nonlinear Sci Numer Simul. 2024;137:108169. doi:10.1016/j.cnsns.2024.108169.
35. Elbar C, Perthame B, Poiatti A, Skrzeczkowski J. Nonlocal Cahn-Hilliard equation with degenerate mobility: incompressible limit and convergence to stationary states. Arch Ration Mech Anal. 2024;248(3):41. doi:10.1007/s00205-024-01990-0.
36. Wu XF, Dzenis YA. Phase-field modeling of the formation of lamellar nanostructures in diblock copolymer thin films under inplanar electric fields. Phy Rev E-Statist, Nonlin Soft Matt Phy. 2008;77(3):031807. doi:10.1103/PhysRevE.77.031807.
37. Cheng Q, Yang X, Shen J. Efficient and accurate numerical schemes for a hydro-dynamically coupled phase field diblock copolymer model. J Computat Phy. 2017;341(9):44–60. doi:10.1016/j.jcp.2017.04.010.

38. Chen L, Ma Y, Ren B, Zhang G. Numerical approximations of diblock copolymer model using a modified leapfrog time-marching scheme. Computation. 2023;11(11):215. doi:10.3390/computation11110215.
39. Li T, Liu P, Zhang J, Yang X. Efficient Fully decoupled and second-order time-accurate scheme for the Navier-Stokes coupled Cahn-Hilliard Ohta-Kawaski Phase-Field model of Diblock copolymer melt. J Comput Appl Math. 2022;403(10):113843. doi:10.1016/j.cam.2021.113843.
40. Wang Y, Xiao X, Zhang H, Qian X, Song S. Efficient diffusion domain modeling and fast numerical methods for diblock copolymer melt in complex domains. Comput Phys Commun. 2024;305(8):109343. doi:10.1016/j.cpc.2024.109343.
41. Bensimon D, Kadanoff LP, Liang S, Shraiman BI, Tang C. Viscous flows in two dimensions. Rev Mod Phys. 1986;58(4):977. doi:10.1103/RevModPhys.58.977.
42. Cao J, Zhang J, Yang X. Fully-decoupled and second-order time-accurate scheme for the cahn-hilliard ohta-kawaski phase-field model of diblock copolymer melt confined in hele-shaw cell. Commun Mathem Statist. 2024;12(3):479–504. doi:10.1007/s40304-022-00298-3.
43. Xu Z, Han Y, Yin J, Yu B, Nishiura Y, Zhang L. Solution landscapes of the diblock copolymer-homopolymer model under two-dimensional confinement. Phys Rev E. 2021;104(1):014505. doi:10.1103/PhysRevE.104.014505.
44. Zhang H, Liu L, Qian X, Song S. Large time-stepping, delay-free, and invariant-set-preserving integrators for the viscous Cahn-Hilliard–Oono equation. J Comput Phys. 2024;499(2):112708. doi:10.1016/j.jcp.2023.112708.
45. Luo W, Zhao Y. Asymptotically compatible schemes for nonlocal Ohta-Kawasaki model. Numer Methods Partial Differ Equ. 2024;40(6):e23143. doi:10.1002/num.23143.
46. Iqbal MJ, Soomro I, Mahar MH, Gulzar U. Exploring long-range order in diblock copolymers through cell dynamic simulations. VFAST Transact Softw Eng. 2024;12(2):31–45. doi:10.21015/vtse.v12i2.1795.
47. Xiao X, Feng X, Shi Z. Efficient numerical simulation of Cahn-Hilliard type models by a dimension splitting method. Comput Mathem Appl. 2023;136(6):54–70. doi:10.1016/j.camwa.2023.01.037.
48. Shams M, Kausar N, Ahmed SF, Badruddin IA, Javed S. Efficient numerical scheme for solving large system of nonlinear equations. Comput Mater Contin. 2023;74(3):5331–47. doi:10.32604/cmc.2023.033528.
49. Eyre DJ. Unconditionally gradient stable time marching the Cahn-Hilliard equation. MRS Online Proc Libr (OPL). 1998;529:39. doi:10.1557/PROC-529-39.
50. Semendyayev IBK, Mühlig GMH. Handbook of mathematics. 3rd ed. Berlin/Heidelberg, Germany: Springer; 1997.
51. Kim J, Kwak S, Lee HG, Hwang Y, Ham S. A maximum principle of the Fourier spectral method for diffusion equations. Electr Res Arch. 2023;31(9):5396–405. doi:10.3934/era.2023273.
52. Xia Q, Yang J, Kim J, Li Y. On the phase field based model for the crystalline transition and nucleation within the Lagrange multiplier framework. J Comput Phys. 2024;513(336):113158. doi:10.1016/j.jcp.2024.113158.
53. Li Y, Lv Z, Xia Q. On the adaption of biological transport networks affected by complex domains. Phys Fluids. 2024;36(10):101906. doi:10.1063/5.0231079.
54. Hwang Y, Ham S, Lee HG, Kim H, Kim J. Numerical algorithms for the phase-field models using discrete cosine transform. Mech Res Commun. 2024;139:104305. doi:10.1016/j.mechrescom.2024.104305.
55. Jeong D, Lee S, Choi Y, Kim J. Energy-minimizing wavelengths of equilibrium states for diblock copolymers in the hex-cylinder phase. Curr Appl Phy. 2015;15(7):799–804. doi:10.1016/j.cap.2015.04.033.
56. Chen C, Zhang J, Yang X. Efficient numerical scheme for a new hydrodynamically-coupled conserved Allen-Cahn type Ohta-Kawaski phase-field model for diblock copolymer melt. Comput Phys Commun. 2020;256(10):107418. doi:10.1016/j.cpc.2020.107418.
57. Yang J, Lee C, Jeong D, Kim J. A simple and explicit numerical method for the phase-field model for diblock copolymer melts. Comput Mater Sci. 2022;205(3):111192. doi:10.1016/j.commatsci.2022.111192.
58. Shin J, Lee HG, Lee JY. Convex splitting Runge-Kutta methods for phase-field models. Comput Mathem Appl. 2017;73(11):2388–403. doi:10.1016/j.camwa.2017.04.004.
59. Dehghan M. Saulyev's techniques for solving a parabolic equation with a non linear boundary specification. Int J Comput Mathem. 2003;80(2):257–65. doi:10.1080/00207160304670.
60. Yang X. Linear, first and second-order, unconditionally energy stable numerical schemes for the phase field model of homopolymer blends. J Computat Phy. 2016;327(4):294–316. doi:10.1016/j.jcp.2016.09.029.

61. Chen R, Gu S. On novel linear schemes for the Cahn-Hilliard equation based on an improved invariant energy quadratization approach. J Comput Appl Math. 2022;414:114405. doi:10.1016/j.cam.2022.114405.
62. Shen J, Xu J, Yang J. The scalar auxiliary variable (SAV) approach for gradient flows. J Computat Phy. 2018;353(11):407–16. doi:10.1016/j.jcp.2017.10.021.
63. Zhang J, Chen C, Yang X. Efficient and energy stable method for the Cahn-Hilliard phase-field model for diblock copolymers. Appl Numer Mathem. 2020;151(1):263–81. doi:10.1016/j.apnum.2019.12.006.
64. Zhang J, Yang X. A new magnetic-coupled Cahn-Hilliard phase-field model for diblock copolymers and its numerical approximations. Appl Math Lett. 2020;107(9):106412. doi:10.1016/j.aml.2020.106412.
65. Wu J, Zhang X, Tan Z. An unconditionally energy stable algorithm for copolymer-homopolymer mixtures. Int J Mech Sci. 2023;238(6):107846. doi:10.1016/j.ijmecsci.2022.107846.
66. Huang J, Ji G. Error estimates of the sav method for the coupled Cahn-Hilliard system in copolymer/homopolymer mixtures. Commun Mathem Sci. 2023;21(7):1895–916. doi:10.4310/CMS.2023.v21.n7.a7.
67. Li Y, Qin K, Xia Q, Kim J. A second-order unconditionally stable method for the anisotropic dendritic crystal growth model with an orientation-field. Appl Numer Mathem. 2023;184(1):512–26. doi:10.1016/j.apnum.2022.11.006.
68. Jiang B, Xia Q, Kim J, Li Y. Efficient second-order accurate scheme for fluid-surfactant systems on curved surfaces with unconditional energy stability. Commun Nonlinear Sci Numer Simul. 2024;135(32):108054. doi:10.1016/j.cnsns.2024.108054.
69. Lai S, Jiang B, Xia Q, Xia B, Kim J, Li Y. On the phase-field algorithm for distinguishing connected regions in digital model. Eng Anal Bound Elem. 2024;168(2):105918. doi:10.1016/j.enganabound.2024.105918.
70. Geng S, Li T, Ye Q, Yang X. A new conservative Allen-Cahn type Ohta-Kawaski phase-field model for diblock copolymers and its numerical approximations. Adv Appl Math Mech. 2022;14(1):101–24. doi:10.4208/aamm.OA-2020-0293.
71. Gerisch A, Chaplain MA. Mathematical modelling of cancer cell invasion of tissue: local and non-local models and the effect of adhesion. J Theore Bio. 2008;250(4):684–704. doi:10.1016/j.jtbi.2007.10.026.
72. Chauviere A, Hatzikirou H, Kevrekidis IG, Lowengrub JS, Cristini V. Dynamic density functional theory of solid tumor growth: preliminary models. AIP Adv. 2012;2(1):11210. doi:10.1063/1.3699065.
73. Horntrop DJ, Katsoulakis MA, Vlachos DG. Spectral methods for mesoscopic models of pattern formation. J Computat Phy. 2001;173(1):364–90. doi:10.1006/jcph.2001.6883.
74. Fife P. Some nonclassical trends in parabolic and parabolic-like evolutions. In: Kirkilionis M, Krömker S, Rannacher R, Tomi F, editors. Trends in nonlinear analysis. Berlin, Heidelberg: Springer; 2003. doi:10.1007/978-3-662-05281-5.
75. Lee C, Kim S, Kwak S, Hwang Y, Ham S, Kang S, et al. Semi-automatic fingerprint image restoration algorithm using a partial differential equation. AIMS Mathematics. 2023;8(11):27528–41. doi:10.3934/math.20231408.
76. Lee C, Jeong D, Yoon S, Kim J. Porous three-dimensional scaffold generation for 3D printing. Mathematics. 2020;8(6):946. doi:10.3390/math8060946.
77. Yoon S, Lee C, Park J, Jeong D, Kim J. Uniformly distributed circular porous pattern generation on surface for 3d printing. Numer Mathem-Theory Meth Appl. 2020;13(4):845–62.
78. Xia B, Xi X, Yu R, Zhang P. Unconditional energy-stable method for the Swift-Hohenberg equation over arbitrarily curved surfaces with second-order accuracy. Appl Numer Mathem. 2024;198:192–201. doi:10.1016/j.apnum.2024.01.005.
79. Li Y, Liu R, Xia Q, He C, Li Z. First-and second-order unconditionally stable direct discretization methods for multi-component Cahn-Hilliard system on surfaces. J Comput Appl Math. 2022;401:113778. doi:10.1016/j.cam.2021.113778.
80. Xia Q, Liu Y, Kim J, Li Y. Binary thermal fluids computation over arbitrary surfaces with second-order accuracy and unconditional energy stability based on phase-field model. J Comput Appl Math. 2023;433:115319. doi:10.1016/j.cam.2023.115319.